Determining permeability tensors of porous media: A novel 'vector kinetic' numerical approach

Yann Jobic, Prashant Kumar, Frédéric Topin, Rene Occelli

Determining permeability tensors of porous media: a novel 'vector kinetic' numerical approach

Y Jobic[1], **P Kumar**[1], **F Topin**[1] **and R Occelli**[1]

[1]Aix-Marseille Université, IUSTI, CNRS UMR 7343

5, Rue Enrico Fermi, 13453 Marseille Cedex 13, France

E-mail: yann.jobic@univ-amu.fr

Abstract. New structurally tailored porous materials are nowadays used in many engineering applications due to several attractive properties. Knowledge of pressure losses or flow structures in such complex media and their relationship with geometrical parameters are thus critical for various applications. Precise determination of local flow behavior and macroscale properties of natural media (soils, biomass....) are increasingly needed. It is therefore important to simulate the complex and unsteady flows by reliable numerical methods and to determine intrinsic macroscopic hydraulic properties on porous structures. The availability of low cost, easy-to use High-performance computational resources lead to generalization of pore scale numerical simulations in various fields. The recent development of innovative scheme like LBM to overcome the classical drawback of commercial softwares (VF, EF) in achieving high accuracy, shows the potential of kinetic based methods for producing efficient and accurate solvers. An alternative vector kinetic method is proposed to solve Incompressible Navier-Stokes equations at pore scale and eventually determine permeability tensors of complex porous media. A moment based (vs discrete velocities), non-diffusive, explicit, parallel implementation was implemented and successfully used on several totally different complex geometries. Excellent results at low Re number were obtained, the method is thus well suited for permeability tensors determination of complex heterogeneous media. The code was validated against classical benchmark as well as experimental and numerical permeability data obtained on different porous media of variable

[1]Y Jobic: yann.jobic@univ-amu.fr.

porosity namely (i) foams (virtual model structures and real samples), (ii) sandstone and (iii) wood.

1. Introduction

Transport phenomena in different porous media have been studied for nearly two centuries. However, the works on high porosity porous media i.e. open-cell foams are still relatively scarce and recent analytical models used for conventional porous media such as packed bed of spheres are not directly applicable on foams (Kumar et al, 2014). Several studies characterizing hydraulic properties of foams have been undertaken to fill this gap. On the other hand, experimental and numerical results characterizing the pressure drop in the foams are highly dispersed (Bonnet et al, 2008). Because of advances in 3D imaging techniques, an emerging trend is the determination of intrinsic hydraulic parameters from flow laws on reconstructed geometries using 3D direct numerical simulations, often using commercial tools (Brun et al, 2009). These tools (e.g. Starccm+, Fluent, Comsol, Pam flow, OpenFoam, etc.) are mature, often allow modelling multiple physical phenomena, and benefit from long term development (more than half a century of continuous intense development for most commonly used numerical approaches like Finite Volumes or Finite Elements). They are nowadays standard engineering tools for many industrial problems as well as development or research ones. Nevertheless, such methods have some drawbacks, as the numerical diffusion, and recent development of both mathematical approaches and computational resource give room for emergence of new numerical methods, namely kinetic method.

Kinetic methods for the simulation of compressible flows have been introduced in the eighties (e.g Pullin, 1980, Reitz, 1981, Mandal et al, 1989). The schemes were derived originally by using the idea of the rescaled Boltzmann Equation (BE): the compressible Euler equations can be obtained as the hydrodynamic limit of the BE (Levermore, 1991, Bardos, 1993). These schemes are called kinetic schemes, Boltzmann schemes, or BGK schemes (for Bhatnagar-Gross-Krook).

The general structure of kinetic schemes that enables entropy compatibility for systems of conservation laws has later been established (Bouchut, 1999), and their equivalence with Flux Vector Splitting (FVS) schemes was proved in Bouchut, 2002. More general relaxation approximations for hydrodynamic systems were proposed in Chen et al, 1994. The use of kinetic schemes with a finite number of velocities (velocities on a lattice in several dimensions), or Lattice Boltzmann schemes have been considered for long, e.g. Boghosian et al, 1987, McNamara et al, 1988, Succi et al, 1989, d'Humières, 1992. The application of the kinetic method to diffusive problems was developed later (e.g. Elton et al, 1995, Jin et al, 1998, Bouchut et al, 2000). For incompressible Navier-Stokes equations, the kinetic method with a finite number of velocities (or Lattice Boltzmann method, LBM) has been intensively used (Succi, 2001).

Meanwhile, the simplicity of LBM has enabled it to be successfully applied to a wide range of problems (Aidun, 2010). LBM used for complex geometries structure such as foams is still challenging (Liu, 2015) and some limitations of the formalism such as numerical instability at low viscosities, (Lallemand et al, 2000) or boundary position dependence on variable viscosity, (e.g. Narváez et al, 2010) has been raised. A lot of efforts have been made to overcome these limitations. For example, dubbed regularized LBM has been developed to improve numerical stability (Succi, 2001). The multiple relaxation time (MRT) collision operator has been used to improve the numerical stability by separating the relaxation rates of the hydrodynamic (conserved) and non-hydrodynamic (non-conserved) moments (d'Humières et al, 2002). Unfortunately, it destroys the entropy compatibility.

The use of special velocity lattices and particular Maxwellians that are not entropy compatible also contribute to the loss of robustness (Chikatamarla et al, 2009). Indeed, as it was shown in Yong et al, 2005, usual LBM (as opposed to entropic LBM, see for instance Karlin et al, 1998, Succi et al, 2002) is not able to comply with any entropy theorem, and the study of stability must be performed with additional difficulties.

Our work takes its roots in (Natalini et al, 2008) where a limited number of velocity directions are used, in accordance with (Bouchut, 2002). Even if we start from kinetic considerations, we use the approach of (Bouchut et al, 2006) to write a simple explicit finite volume/difference scheme on the macroscopic moments themselves, thus finally avoiding the kinetic aspects. This approach enables to analyze the accuracy in a simple way, and lead to simple, and physical interpretation of boundary conditions. Moreover, the implementation requires less memory consumption than a discrete velocities approach. Eventually the explicit scheme insures the good scalability of parallel software implementation. We end up with a BGK-FVS method that is second-order accurate without any special choice of the velocities and with standard forward Euler time stepping. Indeed, it is just the Lax-Friedrichs scheme applied to a scaled compressible isentropic system. It satisfies a discrete entropy inequality under a CFL (Courant Friedrichs Lewy) condition involving only the viscosity, and a sub-characteristic condition that can be interpreted as saying that a cell Reynolds number associated to the grid size is less than one.

As compared to classical LBM type method, this one is non-diffusive, explicit, parallel and successfully used on several totally different complex geometries. Moreover, from practical point of view, the main advantages of our method are:

- Boundary condition implementation is direct and easy (moment-based scheme).
- Explicit stability conditions allow a priori evaluation of mesh/time step requirements.
- The implementation requires less memory consumption than a discrete velocities approach, eventually the explicit scheme insures the good scalability of parallel software implementation.

- The moment base scheme is naturally written in term of physical quantities (obviously it could be made non-dimensional), which could help its use in other communities such as porous media or biomedical domain.

This kinetic approach is presented and used to solve transport equations at local (pore) scale. The macroscopic permeability of the porous media is eventually obtained from volume averaging and correlated with morphological characteristics of different foam samples as well as complex/heterogeneous media.

2. Numerical method

We solve the Incompressible Navier-Stokes Equations (INSE):

$$\begin{cases} \frac{\partial \boldsymbol{v}}{\partial t} + \boldsymbol{v} \cdot \nabla \boldsymbol{v} = -\nabla p + \nu \nabla^2 \boldsymbol{v} \\ \nabla \cdot \boldsymbol{v} = 0 \end{cases}, \tag{1}$$

With $\boldsymbol{v}$ the velocity, ν the viscosity, and p the pressure. We therefore developed a numerical method called "FVS-BGK" which comes from a rigorous use of the kinetic theory. The idea, summarized in Figure 1, is to solve a hyperbolic system of conservation law with a kinetic method based on a BGK collisional operator, approximated by a transport/projection algorithm. The time (explicit Euler) and space discretization are achieved on a constant cell approximation similar to a finite volume method. The discrete velocities are calculated using a 2-D point stencil on a regular structured mesh (e.g. 6 points for 3 dimensional problems). A parabolic rescaling is then applied to the kinetic variables to solve an Incompressible Euler system. Finally, the INSE diffusion term is added by matching the real fluid viscosity to the numerical diffusion of the scheme. The entropy existence is carefully analyzed at each construction step of this method, and gives directly a stability condition, which ensures the existence and uniqueness of the solution. This method is fully detailed in Bouchut et al, 2018.

2.1. Kinetic relaxation to compressible models

We first solve a hyperbolic system of conservation laws, defined as:

$$\partial_t \boldsymbol{W} + \sum_{j=1}^{D} \frac{\partial}{\partial x_j} F_j(\boldsymbol{W}) = 0, \tag{2}$$

with $\boldsymbol{W}$ the vector of unknown (density, velocity) and D the space dimension. We used a kinetic method based on a vectorial BGK (simpler collisional operator of the Boltzmann equation) (Krook et al, 1954). Those kinds of methods add a kinetic variable ξ, which describe the direction of the particle's velocity. It can be written as:

$$\partial_t \boldsymbol{f} + \frac{1}{\epsilon_{adv}} \mathbf{v}(\xi) \cdot \nabla_{\mathbf{x}} f = \frac{1}{\epsilon_{coll}} (\boldsymbol{M}[\boldsymbol{W}] - \boldsymbol{f}), \tag{3}$$

with $\boldsymbol{f}$ the probability density function (pdf), ϵ_{adv} and ϵ_{coll} small positive parameters that will tend to zero in a special way. $\boldsymbol{W}$ is a vector, corresponding to the moments of the Maxwellian equilibrium $\boldsymbol{M}$. For equation (3) to be consistent with (2), we must impose the following conditions to $\boldsymbol{M}$ (which are the mass and flux conservation):

$$\int \boldsymbol{M}[\boldsymbol{W}](\xi) d\xi = 0, \tag{4}$$

$$\int v_j(\xi) \boldsymbol{M}[\boldsymbol{W}](\xi) d\xi = F_j(\boldsymbol{W}), \tag{5}$$

naming F_j the flux of $\boldsymbol{W}$.

The challenging task is then to define $\boldsymbol{M}$ so that the model conserves the good properties of the original kinetic scheme, i.e. a convex entropy η, as well at the continuous level than at discrete level. The chosen form of $\boldsymbol{M}$ is linear with respect to $\boldsymbol{W}$ and F_j. The existence of the associated entropy η (and her flux) will give a special condition, called sub-characteristic condition, which will greatly simplify the stability analysis of the scheme.

2.2. Discrete scheme

We will solve equation (3) by a transport-projection algorithm (Bouchut, 2002). The idea is that in equation (3), if ϵ_{coll} tends toward zero, a bounded solution implies that $\boldsymbol{f}$ tends toward $\boldsymbol{M}[\boldsymbol{W}]$. Therefore, at each step, $\boldsymbol{f}$ is Maxwellian, and thus we can rewrite equation (3) with a change of variables:

$$\begin{cases} \partial_t \boldsymbol{w} + v(\xi) \cdot \nabla_x \boldsymbol{w} = \boldsymbol{0}, \\ \forall \xi, \boldsymbol{w}(t_n, \boldsymbol{x}, \xi) = \boldsymbol{W}^n(\boldsymbol{x}). \end{cases} \tag{6}$$

This algorithm has some interesting features; the most important one is that all the kinetic variables will be eliminated in the final scheme, using only the dimensional macroscopic physical variables (density, velocity). We consider a Cartesian mesh, with a discrete velocity set of 2 times D velocities for ξ, and constant data in each cell as in the finite volume method. Then the transport/projection algorithm is interpreted as a Flux Vector Splitting (FVS) method. That means that the flux is decomposed in separated directions: $\boldsymbol{F}_j(\boldsymbol{W}) = \boldsymbol{F}_j^+(\boldsymbol{W}) + \boldsymbol{F}_j^-(\boldsymbol{W})$. We have chosen the Lax-Friedrichs decomposition in order to define $\boldsymbol{F}_\mathbf{j}^{\pm}(\boldsymbol{W})$ (Bouchut, 2018). This will enable to import the continuous kinetic entropy condition to the discrete level. The resulting scheme, using the above discretization, becomes:

$$\begin{cases} \boldsymbol{W_i^{n+1}} - \boldsymbol{W_i^n} + \frac{\Delta t}{\Delta x}\sum_{j=1}^{D}\left(\boldsymbol{F}^n_{\boldsymbol{i}+\frac{\boldsymbol{e_j}}{2}} - \boldsymbol{F}^n_{\boldsymbol{i}-\frac{\boldsymbol{e_j}}{2}}\right) = \boldsymbol{0}, \\ \boldsymbol{F}^n_{\boldsymbol{i}+\frac{\boldsymbol{e_j}}{2}} = \boldsymbol{F_j^+}(\boldsymbol{W_i^n}) + \boldsymbol{F_j^-}(\boldsymbol{W^n_{i+e_j}}). \end{cases} \tag{7}$$

2.3. Parabolic rescaling

We search the limit of equation (2) using two different steps. We first set $\epsilon_{adv} \approx \sqrt{\epsilon_{coll}}$, which explains why we call it the "parabolic rescaling". We can note that when $\epsilon_{coll} \to 0$, ϵ_{adv} is greater than ϵ_{coll}. We can then fix ϵ_{adv} and let ϵ_{coll} tends toward zero. This limit is well known (Bouchut et al, 2000), and the system in this asymptotic limit tends toward a classical system of conservation laws:

$$\begin{cases} \partial_t \rho + \nabla_{\boldsymbol{x}} \cdot (\rho \boldsymbol{u}) = 0, \\ \partial_t(\rho \boldsymbol{u}) + \nabla_{\boldsymbol{x}} \cdot \left(\rho \boldsymbol{u} \otimes \boldsymbol{u} + \frac{P(\rho)-P(\overline{\rho})}{\epsilon_{adv}^2}\boldsymbol{I}\right) = \boldsymbol{0}, \end{cases} \tag{8}$$

with $\overline{\rho}$ the reference density. We choose the state equation as:

$$P(\rho) = c_s^2 \rho \tag{9}$$

with c_s the speed sound. We want the solution to be bounded when ϵ_{adv} tends toward zero, therefore equation (8) and (9) lead to keep ρ in the neighbourhood of $\overline{\rho}$: $\rho = \overline{\rho} + O(\epsilon_{adv}^2)$

Defining p as the physical pressure by:

$$\rho \to \bar{\rho}, \frac{P(\rho)-P(\overline{\rho})}{\epsilon^2} \to \bar{\rho} p. \tag{10}$$

Therefore equation (7) becomes the Incompressible Euler equations:

$$\begin{cases} \partial_t \rho + \nabla_{\boldsymbol{x}} \cdot (\rho \boldsymbol{u}) = 0, \\ \partial_t(\rho \boldsymbol{u}) + \nabla_{\boldsymbol{x}} \cdot (\rho \boldsymbol{u} \otimes \boldsymbol{u} + p\boldsymbol{I}) = \boldsymbol{0}. \end{cases} \tag{11}$$

2.4. Adding diffusion

To obtain incompressible Navier-Stokes equations (INSE), we need to add the diffusive term. We define the numerical diffusion coming out from the discrete numerical scheme, and fix it accordingly the free parameters of the current scheme to the desired physical diffusion leading to the following formula (consistency):

$$\epsilon = \frac{c\Delta x}{2\nu}. \tag{12}$$

As the scheme is explicit in time, CFL can be described as:

$$2D\frac{\nu \Delta t}{\Delta x^2} \leq 1. \tag{13}$$

Finally, the numerical scheme in terms of density and dimensioned physical velocity is written as:

$$\begin{cases} \rho_{\boldsymbol{i}}^{n+1} = \left(1 - 2D\frac{\nu\Delta t}{\Delta x^2}\right)\rho_{\boldsymbol{i}}^{n} + \frac{\nu\Delta t}{\Delta x^2}\sum_j^D \rho_{\boldsymbol{i}-\boldsymbol{e}_j}^{n} + \frac{\Delta x}{2\nu}(\rho\boldsymbol{u}_j)_{\boldsymbol{i}-\boldsymbol{e}_j}^{n} + \rho_{\boldsymbol{i}+\boldsymbol{e}_j}^{n} - \frac{\Delta x}{2\nu}(\rho\boldsymbol{u}_j)_{\boldsymbol{i}+\boldsymbol{e}_j}^{n}, \\ (\rho\boldsymbol{u})_{\boldsymbol{i}}^{n+1} = \left(1 - 2D\frac{\nu\Delta t}{\Delta x^2}\right)(\rho\boldsymbol{u})_{\boldsymbol{i}}^{n} \\ + \frac{\nu\Delta t}{\Delta x^2}\sum_j^D \left((\rho\boldsymbol{u})_{\boldsymbol{i}-\boldsymbol{e}_j}^{n} + \frac{\Delta x}{2\nu}(\rho\boldsymbol{u}_j\boldsymbol{u})_{\boldsymbol{i}-\boldsymbol{e}_j}^{n} + \frac{2\nu}{\Delta x}\frac{P(\rho_{\boldsymbol{i}-\boldsymbol{e}_j}^{n})}{c^2}\boldsymbol{e}_j \right. \\ \left. + (\rho\boldsymbol{u})_{\boldsymbol{i}+\boldsymbol{e}_j}^{n} + \frac{\Delta x}{2\nu}(\rho\boldsymbol{u}_j\boldsymbol{u})_{\boldsymbol{i}+\boldsymbol{e}_j}^{n} + \frac{2\nu}{\Delta x}\frac{P(\rho_{\boldsymbol{i}+\boldsymbol{e}_j}^{n})}{c^2}\boldsymbol{e}_j \right). \end{cases} \tag{14}$$

For each moment the sum over *j* corresponds to the projection step (f is forced to be Maxwellian). Finally, considering the Cell Reynolds Number:

$$Re_m = \frac{\Delta x}{2\nu}\max_{i,j=1\ldots D}|u_{ij}|. \tag{15}$$

The sub-characteristic stability condition is then:

$$\frac{c_s}{1-Re_m} \leq c. \tag{16}$$

The initialization of parameters is as follows: we fix $\epsilon = 1$ (this parameter having no influence in the final scheme), we find c with the consistency equation (12), we then fix the ratio $c_s/c = 1$ (numerical tests proved this choice to provide good accuracy) giving the last parameter c_s.

The formulation, which is written in term of moments, encompass the kinetic origin of the continuous scheme. The pdfs are Maxwellian at each time step, thus allowing us to write the transport-projection scheme in term of physical macroscopic variables. Eventually, the scheme (equation 14) is implemented similarly to a classical FVM one (see figure 1).

As the scheme is only written in term of moments, the boundary conditions are treated as in FVM or finite difference method. For applying Dirichlet boundary conditions, we use the standard ghost cells method. Some well-chosen values are assigned on an extra cell outside the domain. For example, the wall boundary condition corresponds to setting zero Dirichlet condition to the normal velocity. The ghost cell method is also used for the Neumann boundary condition. The Combinations of Dirichlet and Neumann conditions are also possible, like setting Dirichlet conditions for some components of **W**, and Neumann to the other components (see Bouchut, 2018 for details).

3. Macroscopic equations

3.1. Darcy equation

The first observations of monophasic flows through sand soils (Darcy, 1856) have shown that there is a linear relationship between the pressure drops and the filtration velocity at low Reynolds. The Stokes

equation can be averaged (neglecting the Brinkman correction and gravity) for Darcy's law (Whitaker, 1986):

$$-\overline{\overline{K_D}}\nabla\langle P\rangle^f = \mu_f\langle V\rangle, \tag{17}$$

where μ_f is the fluid viscosity and $\langle V\rangle$ is the average fluid velocity over all the volume of the sample, $\overline{\overline{K_D}}$ is the permeability tensor It is a second order symmetric positive and definite tensor, it's an intrinsic property of the medium and a constant throughout the domain it also does not depend on the shape of the domain.

3.2. Extraction of the permeability tensor

To identify $\overline{\overline{K_D}}$ (a positive defined symmetric tensor) we use the method described in Bear, 1972 and Renard, 2001. A block shaped domain meshed with constant size cartesian 3D mesh was built for each sample either from CAD or tomographic images. We then solve the flow problem (INSE) at pore scale then extract the averaged velocity and pressure gradients. In 3D, one solution at pore scale for a given situation with given boundary condition leads to a system of 3 equations with 3 unknowns (the components of $\overline{\overline{K_D}}$). We use equation 15 to write:

$$\begin{bmatrix} K_{xx} \\ K_{xy} \\ K_{xz} \\ K_{yx} \\ K_{yy} \\ K_{yz} \\ K_{zx} \\ K_{zy} \\ K_{zz} \end{bmatrix} = \begin{bmatrix} \nabla P_x^1 & \nabla P_y^1 & \nabla P_z^1 & 0 & 0 & 0 & 0 & 0 & 0 \\ 0 & 0 & 0 & \nabla P_x^1 & \nabla P_y^1 & \nabla P_z^1 & 0 & 0 & 0 \\ 0 & 0 & 0 & 0 & 0 & 0 & \nabla P_x^1 & \nabla P_y^1 & \nabla P_z^1 \\ \nabla P_x^2 & \nabla P_y^2 & \nabla P_z^2 & 0 & 0 & 0 & 0 & 0 & 0 \\ 0 & 0 & 0 & \nabla P_x^2 & \nabla P_y^2 & \nabla P_z^2 & 0 & 0 & 0 \\ 0 & 0 & 0 & 0 & 0 & 0 & \nabla P_x^2 & \nabla P_y^2 & \nabla P_z^2 \\ \nabla P_x^3 & \nabla P_y^3 & \nabla P_z^3 & 0 & 0 & 0 & 0 & 0 & 0 \\ 0 & 0 & 0 & \nabla P_x^3 & \nabla P_y^3 & \nabla P_z^3 & 0 & 0 & 0 \\ 0 & 0 & 0 & 0 & 0 & 0 & \nabla P_x^3 & \nabla P_y^3 & \nabla P_z^3 \end{bmatrix}^{-1} \begin{bmatrix} {V_x}^1 \\ {V_y}^1 \\ {V_z}^1 \\ {V_x}^2 \\ {V_y}^2 \\ {V_z}^2 \\ {V_x}^3 \\ {V_y}^3 \\ {V_z}^3 \end{bmatrix}. \tag{18}$$

In system 17, subscripts x, y, z describe the directions while superscripts 1,2,3 describe the numerical simulation performed each time in each direction. In case of isotropic foams, diagonal components of permeability tensors are equal while the other components are zero.

To obtain the tensor, we need to solve 3 flow problems with different orientations of the mean flow imposed by the boundary condition, we then have to solve a linear system of 9 equations and 9 unknowns. We choose to prescribe pressure difference between two opposite faces of the domain while other faces were set as symmetry planes. This was done 3 times with the pressure difference imposed successively along $\boldsymbol{x}$, $\boldsymbol{y}$ and $\boldsymbol{z}$.

3.3. Determination of principal directions

Two additional treatments are introduced to check the quality of the results and eventual bias induced by the extraction method:

- We suppress the « numerically induced» very low gradients (< 1/1000 main gradient) to avoid the apparition of non-physical term linked to matrix inversion. These terms appear in directions perpendicular to the main flow. Generally speaking, this phenomenon occurs for weakly anisotropic objects. The order of magnitude of these gradients is comparable to the numerical accuracy of the results. In some cases, taking them into account leads to non-physical results. Their suppression is natural in these cases. We systematically assess the impact of their removal on the final result. It has been found that only the non-diagonal terms were changed.
- We force the symmetry of the permeability tensor. The equations (19) below are combined with the system (18), thus leading to 9 equations 6 unknown over-determined system (20).

$$\begin{cases} K_{xy} = K_{yx} \\ K_{xz} = K_{zx}, \\ K_{yz} = K_{zy} \end{cases} \tag{19}$$

$$\overline{\overline{K_D}} = \begin{bmatrix} {K_D}^{xx} \\ {K_D}^{xy} \\ {K_D}^{xz} \\ {K_D}^{yy} \\ {K_D}^{yz} \\ {K_D}^{zz} \end{bmatrix} = \mu_f \begin{bmatrix} \nabla P_x^1 & \nabla P_y^1 & \nabla P_z^1 & 0 & 0 & 0 \\ 0 & \nabla P_x^1 & 0 & \nabla P_y^1 & \nabla P_z^1 & 0 \\ 0 & 0 & \nabla P_x^1 & 0 & \nabla P_y^1 & \nabla P_z^1 \\ \nabla P_x^2 & \nabla P_y^2 & \nabla P_z^2 & 0 & 0 & 0 \\ 0 & \nabla P_x^2 & 0 & \nabla P_y^2 & \nabla P_z^2 & 0 \\ 0 & 0 & \nabla P_x^2 & 0 & \nabla P_y^2 & \nabla P_z^2 \\ \nabla P_x^3 & \nabla P_y^3 & \nabla P_z^3 & 0 & 0 & 0 \\ 0 & \nabla P_x^3 & 0 & \nabla P_y^3 & \nabla P_z^3 & 0 \\ 0 & 0 & \nabla P_x^3 & 0 & \nabla P_y^3 & \nabla P_z^3 \end{bmatrix}^{-1} . \begin{bmatrix} {V_x}^1 \\ {V_y}^1 \\ {V_z}^1 \\ {V_x}^2 \\ {V_y}^2 \\ {V_z}^2 \\ {V_x}^3 \\ {V_y}^3 \\ {V_z}^3 \end{bmatrix}. \tag{20}$$

We systematically compare the 3 tensors (full tensor (FT), symmetric (S), without small gradient(WSG)) and results are always similar. Note that the overdetermined system is solved to the last square sense. For all tested cases, the diagonal terms do not change significantly (usually less than 0.1%) while the other terms may change more significantly.

In all cases, we compute eigenvalues λ_i and associated Eigenvectors $\boldsymbol{w}_i$ of the tensor which constitute principal values and direction of the permeability (Bear, 1972):

$$\overline{\overline{K}}_D \times \boldsymbol{w}_i = \lambda_i \boldsymbol{w}_i. \tag{21}$$

This decomposition is useful for comparing the tensor characterizing different samples as the value in the (arbitrary defined) basis of original samples are not comparable. We will also test the

orthogonality of the $\boldsymbol{w}_i$ vectors. If these are orthogonal, then in the basis composed of the $\boldsymbol{w}_i$ vectors, the permeability tensor will be orthotropic, with λ_i as elements of the diagonal.

Moreover, the values of $\boldsymbol{w}_i$ will give an information about the orientation of the original basis (i.e. the basis associated to the real sample and its 3D images) compared to the one composed of the eigenvectors. As it is generally impossible to know beforehand the orientation of permeability tensor, the basis used during either experiments or 3D image acquisition is arbitrary oriented relative to the permeability one. Determining principal basis give the real orientation of the permeability tensor and allow direct comparison between samples or measurement methods as well as correlate anisotropy of such tensor to physical phenomena.

3.4. First application example: Permeability tensor of sandstone

We consider a sandstone sample of porosity 13.5 % (see section 4.3 for details). The first step is to solve system (18). We obtain:

$$\overline{\overline{K}}_{FT} = \begin{pmatrix} 9.75 & 0.355 & 0.236 \\ 0.293 & 7.76 & -0.138 \\ 0.791 & 0.149 & 7.49 \end{pmatrix} \times 10^{-13}\, m^2, \tag{22}$$

with the eigenvalue/eigenvector decomposition in table 1. The second step is to nullify the very low gradient induced by residual numerical noise. We then have the following permeability tensor:

$$\overline{\overline{K}}_{WSG} = \begin{pmatrix} 9.75 & 0.354 & 0.236 \\ 0.293 & 7.76 & -0.139 \\ 0.791 & 0.149 & 7.49 \end{pmatrix} \times 10^{-13}\, m^2, \tag{23}$$

with the eigenvalue/eigenvector decomposition in table 2. In this case, the tensor is nearly identical to the previous one as expected because numerical noise is low on these calculations. Note that in both case the tensors are not symmetrical. This is due to numerical error during inversion, linked to the low degree of anisotropy and the fact that principal direction basis is close to the image one. Finally, we force the symmetry of the tensor (system 20). Then new tensor is then:

$$\overline{\overline{K}}_{S} = \begin{pmatrix} 9.78 & 0.306 & 0.508 \\ 0.306 & 7.74 & -0.0092 \\ 0.508 & -0.0092 & 7.49 \end{pmatrix} \times 10^{-13}\, m^2, \tag{24}$$

with the eigenvalue/eigenvector decomposition in table 3. For all the cases, we checked that the eigenvector basis is orthogonal, giving the final permeability tensor:

$$\overline{\overline{K}}_{D} = \begin{pmatrix} 9.92 & 0 & 0 \\ 0 & 7.71 & 0 \\ 0 & 0 & 7.37 \end{pmatrix} \times 10^{-13}\, m^2, \tag{25}$$

in the $\{\boldsymbol{w}_1, \boldsymbol{w}_2, \boldsymbol{w}_3\}$ basis. See Table 9 for eigenvalues and eigenvectors.

The tensors obtained using the 3 cases are close; indeed, forcing the symmetry induce a small change (~1%) on diagonal terms. Nevertheless, this tensor is symmetric by nature thus the difference are probably dues to numerical error during inversion process.

As the λ_i are relatively close (only 25.8% of relative difference), we can conclude that the sandstone is only slightly anisotropic (and this anisotropy is generally not characterized in experimental studies due to technical limitations). Moreover, it appears clearly that permeabilities along $\boldsymbol{w}_2$ and $\boldsymbol{w}_3$ are very close, which mean that the sample structure characteristic size is significantly different only along the other direction $\boldsymbol{w}_1$. This could be linked to the formation of this natural rock under influence of gravity that lead to a compression along one direction.

The present study focuses only on Darcian regime although the inertial effects can be significant even at low Reynolds number and a Forchheimer law (quadratic relation between velocity and pressure gradient) may be a more accurate model for fluid flow. It is necessary to determine permeability in Darcy regime and check the flow regime based on explored velocity range to choose the flow law in a coherent way (Kumar et al, 2014). In case of non-Darcy flow, equation (16) could be used considering an apparent (velocity dependent) permeability tensor. This latter is constituted by the sum of two tensors, the first one being the Darcian permeability tensor, and the second one relative to the inertia effects (see Soulaine, 2014 for a detailed discussion). The procedure used here could thus still be applied and the flow law parameters are essentially extracted in the same way although some additional complexity arise due to the inertia terms dependency on both magnitude and relative orientation of the velocity.

We validate the computed permeability against literature permeability data (see Hugo et al, 2012; Vicente et al, 2006; Zinszner et al, 2007 and Talon et al, 2006) for two different kinds of samples: a high porosity metallic foam (manufactured medium) as well as a sample of low porosity natural medium, a Fontainebleau sandstone. We then study the influence of geometrical anisotropy (elongation) on the permeability tensor using Kelvin-like structure unit cells, which are simultaneously elongated and compressed differently for each direction. Finally, we study the permeability tensor of a piece of wood (redwood tree).

4. Global hydraulic results

The pore scale numerical method has been extensively validated against classical CFD (Computational Fluid Dynamics) benchmarks such as Poiseuille flow and Taylor-Green vortex problem, which are analytical ones (Jobic, 2016). We also use numerical Benchmarks as the backward facing step flow and the Von Karman vortex shedding over a square obstacle. Those benchmarks results showed that this method is well suited for relatively low Reynolds number (less than 100) to achieve excellent

accuracy on relatively "small" meshes. At higher Reynolds, the cell number should be increased (equation 15), and therefore computing cost may become prohibitive compared to other methods.

We perform some extensive calculations on real domains reconstructed from micro-tomographic images (µCT) as well as over idealized domains, which are by construction already discrete and fixed. The original image resolution defines the maximum Reynolds number compatible with adequate accuracy. And thus, limit the present work to the Darcy regime. The dimension of representative volume element (side >5 cell size) to perform numerical simulations was chosen to optimize results' reliability and computational time (see Brun et al, 2009). The simulations were stopped when K_D converge asymptotically with less than 0.1% variation. Moreover, we also systematically checked mass in-balance at pore scale both over the entire domain (i.e. between inlet and outlet) and between several cross sections inside the domain. Additionally, we also analyzed qualitatively the local velocity pattern looking for local aberrations (e.g. in highly deformed zone of natural media).

4.1. Periodic-idealized Kelvin-like cell

The final purpose of this work is to find a good correlation between some quantitative easily measurable geometrical parameters and the intrinsic permeability property without carrying out 3D numerical calculation on a case-by-case basis. (see Kumar et al, 2017).

To produce such correlations, a permeability database has to be created along with a morphological one. A representative simplified structure (here kelvin-like unit cell) was chosen, then several key geometric parameters such as strut cross-section, porosity, strut and cell size, were varied individually. On each of these virtual samples, we solve Navier-Stokes equations and extract macro-scale properties. At first, we study structure with constant diameter struts then extend this analysis to variable cross-section along the strut axis.

4.1.1. Constant cross section ligament

The computational domain is built from a 3D CAD model generated using the inbuilt function of commercial software, StarCCM+. The foam structure is constructed simply by extruding a sketch along the edge of a truncated octahedron. The sketch (circle of diameter d_s corresponding to strut diameter) is set at the midpoint between 2 nodes of polyhedron and orthogonal to the node-to-node line. It was then swept along this half-strut skeleton up to the node. This procedure is repeated from the four half-struts intersecting at a node. Then, the planes bisecting each angle -constituted by a pair of struts and parallel to the third one- were used to slice the excess length of each strut. These 4 half struts structure were iteratively duplicated by symmetry along the original sketches until a whole cell (plus additional outward half-struts) was constituted. Further, a Boolean intersection with the cubic unit cell is realized.

This procedure was fully parameterized in terms of strut diameter and cell size (Figure 2-left). As the influence of the unit cell size own permeability -K~ $d_{d_{cell}}^2$ - is already well known, (see. Bonnet, 2008) the node-to-node length ($L_N = \sqrt{2}$ mm) is kept fixed for entire calculations giving a fixed cell size ($d_{cell} = 2\sqrt{2}L_N$ =4 mm).

Based on the construction method described above, strut diameter has been used as a control parameter to generate foams of chosen porosities. This allows creating only (in a periodic unit cell) 36 struts that are along the edge of the truncated octahedron. Note that, the strut ligament diameter does not vary along its axis (Figure 2-left). Upon increasing the diameter of the strut, one would reach a point where the structure degenerate and will not be a foam anymore (i.e. the centerline skeleton of the created shape will differ from the truncated octahedron, and some faces between adjacent pores may collapse). We increase progressively the size of strut diameter until the shape degenerates. This point is referenced as a limiting porosity, below which Kelvin-like foam structure having circular cross-section does not exist anymore.

The morphological parameters of virtual Kelvin-like foam structures are numerically measured from CAD data (surface and volume of the structure) and thus, do not induce any significant bias (see Table 4). Note that, the same base mesh size (mesh cells average size) is used for all CFD calculations. Nevertheless, the mesh is constructed for each strut size and local refinement is used to capture properly the geometrical features of the sample.

4.1.2. Influence of mesh resolution

We carried out a detailed study of mesh convergence. There are 2 different aspects that play a role in this case. The CAD mesh used to generate the geometry and the cartesian regular grid on which VFS-BGK calculations are done. This latter is dependent on the quality of the CAD one. As expected, coarse meshing does not provide accurate results as morphological errors are very important. Then the results converge with mesh resolution. Finally, over-meshing lead to adverse results mainly linked to numerical limits of the CAD mesher (numerical accuracy, and creation of poorly conformed cells in small acute zones. These latter lead to generations of unrealistic very small surface corrugations). Consequently, the procedure reaches the point where geometrical structure is poor and INSE solver becomes prohibitively time consuming.

The first step is to verify the impact of the geometric discretized resolution (voxel size) on porosity (ε_0), surface porosity (ε_{surf}), specific surface area (a_c) and permeability (K_D) values of the Kelvin-like foam sample of cylindrical strut shape ($\varepsilon_0 = 0.6$ and 0.95) as presented in Figure 3

It can be observed that the morphological parameters start to converge at higher resolution to capture precisely the 3D foam structure reported in the works of (Kumar et al, 2014). On the other hand, the

main flow topology is well captured despite the lack of resolution (stairs effect as shown in Figure 4). It is a well-known phenomenon (see Inamuro et al, 1997; Clague et al, 2000; Bernsdorf, 2008), which comes from the fact that the specific surface area is nearly the same for all resolutions.

As expected, the calculated permeability converges when mesh resolution increases. To perform parametric studies, a domain constituted of 160^3 mesh cells is chosen to perform CPU/memory cost optimized numerical simulations without compromising significantly accuracy of the data (see Table 6).

4.1.3. Variable cross section ligament

We extended our analysis to variable diameter ligament (Figure 3). The foam structure is constructed in the same way than the constant diameter one. The only difference being that the initial sketch (circle of diameter $d_{s,2}$ corresponding to strut diameter at the middle of strut) is set at the midpoint between 2 nodes and orthogonal to the strut axis. It was then swept along this half-strut skeleton with a draft angle up to the node. Again, his procedure was fully parameterized in terms of strut diameter, cell size and, draft angle (Figure 2-right). Here, the draft angle is positive and mean outward draft during extrusion. It thus led to produce a structure with a bigger strut diameter ($d_{s,1}$) near the node junction while a smaller diameter ($d_{s,2}$) at the middle of the ligament. Such ligament occupies a large volume at node intersections while a small volume at the center of the ligament. This allows us to vary for example the strut size (average) at constant porosity and cell size by changing the draft angle. We also now dispose of representative cells for the most commonly encountered type of solid foams commercially available and used in various industry fields.

Remark: Measurements on real foam samples from different producer clearly shows that according to the manufacturing process (e.g. coating for ceramic one, electrodeposition for metals) solid foam may or may not exhibit “lump” in the vicinity of node junction. Also, several strut cross sections could be produced, and variations of strut diameter are observed or not, either from intentional manufacturing technique (in case of additive fabrication for example) or simply as a consequence of a cost optimized production for specific applications.

The morphological parameters i.e. strut diameter at the middle of ligament ($d_{s,2}$), porosity (ε_o), specific surface area (a_c), and pore diameter (d_p) of 32 virtual Kelvin-like foam samples using classical CAD approach are measured (see Table 5).

4.1.4. Results and discussion

The current numerical results obtained from VFS-BGK on structured grid were compared against numerical results of Kumar et al, (2014) obtained on commercial software (StarCCM+) on polyhedral unstructured mesh.

The classical formula of Ergun, 1952: $K_D = \frac{D_p^2 \epsilon^3}{150*(1-\epsilon)^2}$ (where D_p is equivalent particle diameter) is also compared to these results as it is often used for foam permeability prediction. This latter was originally developed for packed bed of spheres and there is no real agreement in literature about its use (and exact formulation) for the case of foam. Most commonly, permeability was linked to two parameters i.e. pore size and porosity for isotropic and commercially available foams.

Table 7 present several calculated permeability values using FVS-BGK method on constant as well as variable cross section of foam samples.

Our data are in perfect agreement with those from Kumar and Topin, 2014 for the constant strut Kelvin cells (Figure 5). We can note that (Kumar et al, 2014) used a nonstandard Darcy formalism, by considering the mean pressure gradient on the bulk phase, not on the fluid phase (see equation 16). Therefore, a scaling factor (surface porosity) has been applied to their results to retrieve the permeability value with the exact definition. On figure 5 the porosity offset between the 2 dataset is due to the difference in geometric discretization of the original images and is a function of resolution. The proposed discretization method causes errors at the walls according to the resolution where original solid-fluid interfaces are not aligned with voxel faces (figure 4).

The second important point is that the Ergun-like formulation clearly (i) is out of range and (ii) do not follow the same trend than measured/calculated data and thus, cannot be applied -in this form- to open-cell foams. Note that on Figure 5 the Ergun formula values are out of range and have been graphically rescaled to compare the shape of the curve with the actual data.

Several experimental works are reported in term of Ergun 'like formulation. As the available foam sample cover a very narrow range of porosity (typically 0.85 -0.95) - also pore/struts shape may depend on cell diameter - no experimental study covers a wide range of porosity. Thus, for the limited accessible range, the Ergun formulation was adapted using a specific "pore diameter" -different depending on case study - and the discrepancy between Ergun formulation and Foam permeability behavior in respect with porosity was not apparent.

4.2. Real high porosity foam samples

Metallic foams are a class of materials that are attractive for numerous applications, as they present high porosity, high effective thermal conductivity of the solid phase and of the bulk samples. Moreover, they also promote mixing and have excellent specific mechanical properties. Metallic foams are thus used in the field of compact heat exchangers, reformers, two-phase cooling systems, and spreaders. Foams have also been used in high-power compact batteries and catalytic-reactor applications such as fuel cell systems (see e.g. METFOAM, 2015).

A commercial foam sample (NC 1723 Recemat foam see Figure 6a) has been chosen as previous experimental and numerical studies of pressure drop are available (Bonnet, 2008, Brun, 2009). The geometry has been reconstructed from the μCT tomographic images using 198x198x342 voxels.

It appears clearly that these foams present a rather low specific surface, a large pore diameter, and a very high porosity in comparison to classical porous media. It has been demonstrated (Vicente et al, 2006) that the cells are spatially organized (common mean orientation) but some defects appear in this arrangement. Cells of different orientation and size materialize these defects. They appear to accommodate topological constraints associated with plateau border angles, space filling, and constraints produced by manufacturing processes. The corresponding computing domain incorporates those defects, in order to include the representative elementary volume (REV), as in (Brun et al, 2009).

It is important to note that, we have the used the same real sample for the experimental and numerical studies. The numerical domain is however a fraction of the experimental one. This is due to the chosen voxel size for μCT imaging (necessary to capture strut geometry), which leads to a limited field of view. A representative elementary volume of 1.1 × 1.1 × 2 cm3 was used.

We compare our results against different literature data:

1. Experimental data (Bonnet et al, 2008), extrapolated by a Forchheimer law, which finds $K_F = 2.23 \times 10^{-8}$ m^2 (here, K_F represents Forchheimer permeability and is not Darcian permeability, see Kumar and Topin, 2017).
2. Numerical data, also using a Forchheimer law, giving $K_F = 2.8 \times 10^{-8}$ m^2 for an LBM code, and $K_F = 5.6 \times 10^{-8}$ m^2 for a Finite Volume code (E. Brun, 2009). The discrepancy between this latter value and the other one is attributed to data treatment and boundary conditions handling.

Using BGK-FVS scheme, we found $K_D = 3.03 \times 10^{-8}$ m^2(see figure 6). An excellent agreement is obtained with both experimental and numerical results. Note that the pressure gradient versus velocity curve is a perfect line (R^2 = 1.00, Figure 6b), as expected for Darcian regime, showing that the viscous flow is indeed well captured. In literature, the reported permeability (either experimentally or numerically obtained) is often Forchheimer permeability (see Kumar and Topin, 2017), while the permeability obtained here is Darcian permeability. It is difficult to assess accurately the bias between Darcian and Forchheimer permeability, which explains the small differences. However, as the raw data generated using the in-house Finite Volume code are available, we calculate the Darcian permeability from original pressure and velocities data in order to obtain a more representative comparison with our calculations. We obtain $K_D = 2.98 \times 10^{-8}\ m^2$ (figure 7). The relative difference for this permeability and the one obtains with the BGK-FVS method is at about 1.6%, showing an excellent agreement.

Applying the methodology described in Section 3 for the determination of the permeability tensor, we find, the permeability tensor in the basis $\{\boldsymbol{w}_1, \boldsymbol{w}_2, \boldsymbol{w}_3\}$:

$$\overline{\overline{K}}_D = \begin{pmatrix} 3.32 & 0 & 0 \\ 0 & 3.13 & 0 \\ 0 & 0 & 3.14 \end{pmatrix} \times 10^{-8}\, m^2. \tag{26}$$

We have $\max_{i,j,i\neq j} |w_i \cdot w_j| = 1.86 \times 10^{-13}\, m^2$. That means that the principal basis composed of the eigenvectors is orthogonal, and, the basis orientation is very close to the one of the tomographic images. As the foam cells come from the bubbles produced during the foaming of the original polymer precursor that are aligned with the main direction of original bloc (and gravity) this indicates (for this sample) that the manufacturing process respect this orientation. A careful visual analysis of all our sample sheets has shown that their faces are nearly parallel to cell alignment.

The values of the eigenvalues and eigenvectors can be found in Table 8. As the diagonal terms of the tensor λ_i are very close (only 5.7% of relative difference), we can conclude that the NC1723 sample is only slightly anisotropic. From geometrical point of view this foam is also nearly isotropic and cells are slightly elongated along one direction only (see. Brun, 2009). The structure of permeability tensor that exhibit the same trend is clearly governed by the pore characteristic size along its principal axes.

4.3. Low porosity natural media sample

The Fontainebleau sandstone is often used as a benchmark, because of the exceptional quality of the porosity/permeability relation (27) given by Zinszner et al, 2007.

A μCT image of 500^3.voxel – 3x3x3 mm^3, spatial resolution 6 μm – was acquired from a core sample of porosity 14.5%. After normalization and filtering, the grey-level density 3D image was binarized to segment pore and solid volume using a threshold set at the minimum between the two peaks of the gray level histogram (Talon et al, 2006). The binarized sample presents a porosity of 14.1%. The difference with the core bulk porosity could be attributed to both heterogeneity of the sample (μCT image is only a small fraction of the core) and bias linked to the thresholding process.

We then use a bloc of side 1.2 mm^3 - porosity 13.5%- about 1/8 of the original image, to produce a 200^3 cells mesh (figure 8a). The flow problem was solved, and permeability tensor was extracted (see section 3).

We can compare the permeability values to literature experimental data or correlation. An experimental law corresponding to a Fontainebleau sandstone is given in (Zinszner, 2007), which is:

$$\log K_D = a(\log \epsilon)^3 + b(\log \epsilon)^2 + c(\log \epsilon) + d, \tag{27}$$

with the parameters values in Table 10. In this expression, the porosity ϵ is expressed in percentages and gives the permeability in mD. Talon et al, 2006 give the confidence interval of this law (RMSE=0.31), for porosity 14.5%.

For example, it gives the following experimental permeability, for a porosity of 13.5%, $K_{exp} = 5.68 \pm 1.76 \times 10^{-13}\ m^2$. We have however no information on the flow direction used to create the power law function. Permeability values associated to the porosity of the sample at different stage of the analysis have been synthesized in Table 11.

On Figure 9, we compare the permeabilities computed with the BGK-FVS method with the experimental values given by Talon, (2006). Unfortunately, our method could not be tested against the other samples that were not available for a more detailed comparison. The calculated values are in good agreement with experimental one, although these latter are widely spread and exhibit some clear uncertainties both for porosity and permeability.

4.4. Application to anisotropic tailored media (orthotropic case)

Based on the comparison and validations performed on idealized and real open cell foams of different porosities, the proposed method gives reliable permeability values. It can thus be very interesting to obtain permeability tensors on orthotropic foams, as available literature data are very scarce (see Hugo, 2012). Moreover, anisotropic materials could be used to optimize many components or system. For example, tailoring high permeability in one direction while keeping a slightly lower one in the other would be very interesting for heat sink design (e.g. electronic cooling applications).

Orthotropic anisotropy of the original foam sample was realized by elongating and compressing simultaneously in two orthogonal directions by a factor $\sqrt{\Omega}$ and $1/\sqrt{\Omega}$ respectively while the third direction is kept unaffected to conserve porosity. Some anisotropic Kelvin-like foam samples presenting circular strut shape are shown in Figure 10, as well as fluid velocity field (sections in the $\boldsymbol{x}$, $\boldsymbol{y}$ and $\boldsymbol{z}$-directions).

The calculations were repeated imposing the flow successively along the three directions to determine permeability tensors. Results are presented in Figure 11 and Table 12. First, the case where $\Omega = 1$ is isotropic by construction, meaning that $K_{xx} = K_{yy} = K_{zz}$. Moreover, also by construction, the basis composed of the eigenvectors is identical to the one of the computing domains, namely $\{\boldsymbol{e}_1, \boldsymbol{e}_2, \boldsymbol{e}_3\}$. We have then $K_{xx} = Kw_1$, $K_{yy} = Kw_2$, $K_{zz} = Kw_3$.

The result's interpretation of the permeability variation as a function of the deformation is complex as the geometry and the foam angles are varying for each case. It can however be observed that:

- for $\Omega \in [1,2]$, the x-direction permeability increases with elongation deformation, while along the other two directions (i.e. y and z) the permeability decreases (due to the compression deformation).
- for $\Omega \in [2,9]$, the permeabilities along all directions are decreasing. This could come from the increase of the specific surface area or the effect of struts orientations and cross section deformation.

These first results validate the use of the BGK-FVS method for this class of problems; a systematic study of deformation vector on permeability tensor is carried out and will be the object of further publication.

4.5. Complex real geometries: determination of a wood sample properties

4.5.1. Generation of computing domain from raw images

We obtained the image data from LBNL (Lawrence Berkeley National Laboratory) in the frame of the ESM effort at NASA, thanks to Francesco Panerai. It is microtomographic images of redwood sample coming from Mendocino forest, California. The whole sample contains 1800^3 cells, which represent a volume of 5.8 mm^3 (see raw images on Figure 12a for example). Obviously, there is no certainty that this particular sample is representative enough to extract properties of the wood as a material. On the other hand, it could be used to check our INSE solver capability as well as our method of permeability characterization on a complex medium.

Binarization from direct thresholding on the raw data gives unsatisfactory results, as shown in Figure 12b. We can observe a lot of small isolated white voxels (false solid voxels). These speckles come from artefact during image acquisition and need to be suppressed to correctly reconstruct the sample geometry.

We used the iMorph (http://www.imorph.fr/, Brun et al, 2008) software developed at IUSTI, in order to clean up the data and reconstruct the 3D topology. The first treatment was to apply a median filter, which suppress the speckle noise, and then we only conserved the connected components, thus suppressing the free unconnected false solid voxels that are obviously artefacts.

Moreover, as shown in Figure 12a, the images seem mis-oriented compared to the wood apparent structure. A rotation (50 degrees) around z axis has been applied to align visible structure with basis directions. We show with Figure 12c an example of cleaned images. One could clearly observe the suppression of the unwanted voxels.

As it is a recurrent problem in µCT reconstruction, it is interesting to highlight the sensibility of the porosity value to the threshold level during binarization. We plot the cumulative normed histogram of the gray level of the sample image (Figure 13). We observe a strong porosity variation (from 85.7% up

to 89%) for a 5% variation of the threshold. Choosing the right threshold is tricky (as there is often no independent comparable porosity data) and this value has a great influence on the resulting mesh.

Eventually, the whole sample computational domain represents 23 billion of unknowns (1800^3 cells with four unknowns per cells), which is difficult to solve considering the current available computing power.

We have therefore chosen to work on subdomain of smaller size and cut three different domain, at different location of the sample. The first one is a cube of 150 cells edges. As expected, the computing time is very low (37 minutes on 96 processors). The post-processing is easy. However, this subdomain is not representative of the sample (it is not a Representative Element Volume, REV).

The second subdomain is a cube of 200 cells edges and is taken at another (non-overlapping) arbitrary location. The last one is a cube of 600 cells edges that overlaps partially the previous ones, which represent the third of the original sample along each direction or 1/27 of sample volume; see Table 13 for a general presentation of the samples).

For each subdomain, we study its homogeneity, and determine the permeability tensor to check the properties at different scale and try to quantify the representative elementary volume size for such material.

4.5.2. Subdomain 1: 150^3 cells

The homogeneity of the subdomain was analyzed first. We extract 2D porosity of 3 planes that were swept across the entire domain. This operation was realized for 3 perpendicular planes corresponding to each face of the subdomain. The results are reported on figure 14a, the abscissa is the position of the plane relative to its original position.

We first note that the porosity variation of the z direction has less amplitude than the other two. This comes from the fact that the vessels (or pores) are organized by cells that transport the sap in the hardwoods. They are located longitudinally in the timber and may or may not be juxtaposed. In our sample, they are oriented in the z direction.

Moreover, we clearly observe, still in Figure 14a, that near the corner of the sample away from the origin, the porosity is abnormally high. As shown on Figure 15a, this is due to a default in the subdomain -a big hole- leading to two different structures in the region of interest. The first one has a kind of regularity in the vessel organization, the other part contains only the hole. Plotting the contour of the flow in this subdomain confirms (Figure 15b) that the velocity is higher in the region containing the hole. As this default is a local artefact and not a feature of the whole sample, this first subdomain is probably not representative of the whole sample.

Applying the methodology described before for the determination of the permeability tensor, and for simplicity rename the $\{\boldsymbol{w}_1, \boldsymbol{w}_2, \boldsymbol{w}_3\}$ basis by $\{\boldsymbol{x},\boldsymbol{y},\boldsymbol{z}\}$. The permeability tensor in this basis is then:

$$\overline{\overline{K}}_D = \begin{pmatrix} 1.43 & 0 & 0 \\ 0 & 6.65 & 0 \\ 0 & 0 & 9.72 \end{pmatrix} \times 10^{-11}\, m^2, \tag{28}$$

with the values of the eigenvalues and eigenvectors in Table 14. The anisotropy, as expected, is very high, with more than 30% difference between the $\boldsymbol{z}$ and $\boldsymbol{y}$ direction, and a ratio superior to six between the $\boldsymbol{z}$ and $\boldsymbol{x}$ direction. The flow is much easier in the $\boldsymbol{z}$ direction, the one of the vessels. There is however a significant difference between the $\boldsymbol{x}$ and $\boldsymbol{y}$ direction. This indicates that opening size measured in plane $\boldsymbol{x}$-$\boldsymbol{z}$ are smaller than in plane $\boldsymbol{y}$-$\boldsymbol{z}$. This is probably linked to the natural growth of the wood microstructure. These results indicate that we are able to solve INSE equations and extract a permeability tensor from a complex heterogeneous sample.

4.5.3. Subdomain 2: 200^3 cells

The homogeneity of the 200 cells edge's subdomain was again checked (Figure 14b). We observe two small special regions, where the porosity is quite low, at around 75%. However, those two regions are very limited in space compared to the subdomain size (and some similar region were found at other location in the whole sample). Unlike the previous one, this subdomain is not composed of two regions, and look way more homogeneous, as a confirmation of the homogeneity study. Moreover, the porosity along the $\boldsymbol{z}$ axis is quite regular, between 84 and 88 %, which is an expected behavior due to vessels orientation along $\boldsymbol{z}$ direction (see Figure 16a). We can conclude that this subdomain is probably representative of the whole sample, at least more representative than the previous one.

Figure 16b -with a different view angle from 16a to show a small hole in the sample- shows iso-contours of the velocity magnitude field for a pressure gradient (and thus a main flow) imposed along $\boldsymbol{z}$ direction. These iso-contours are mainly tubular, the flow is similar to Poiseuille flow in parallel tube as expected from the wood structure. Nevertheless, patterns, characteristic of tube connection, are visible near the front vertical edge of the view.

Figure 17 shows iso-contours of velocity magnitude for a gradient imposed in transverse direction. In this case, we lose the tubular behavior of the velocity magnitude, for a more erratic one. The fluid crosses the sample by passing from one vessel to the other across opening (of smaller dimension than the vessel) that are not aligned.

We determined the permeability tensor in the $\{\boldsymbol{x},\boldsymbol{y},\boldsymbol{z}\}$ basis:

$$\overline{\overline{K}}_D = \begin{pmatrix} 2.22 & 0 & 0 \\ 0 & 3.83 & 0 \\ 0 & 0 & 7.72 \end{pmatrix} \times 10^{-11}\, m^2, \tag{29}$$

with the values of the eigenvalues and eigenvectors in Table 15. This tensor is slightly different from previous one. There is nearly a factor two between the z and y direction, and a factor 4 between the z and x direction. We can still recover the fact that the vessels are oriented in the z direction. We can conclude that our method captures well the main feature of flow field and relation of permeability tensor with geometrical feature even for complex situations.

4.5.4. Subdomain 3: 600^3 cells

The same analysis was repeated to the biggest subdomain. Figure 14c shows a different porosity behavior than the previous ones, as the variation around the mean porosity value is clearly lower. The subdomain 1 and 2 present porosities varying between 73% and 93%. For subdomain 3, the porosity variation amplitude is nearly 2.5 time lower (82% to 90%). This clearly indicates that the first 2 subdomains are representative of a local zone and not of the whole sample.

The x and y directions present oscillations around the z axis, retrieving again the vessels orientation in the z direction (see Figure 18a).

We do not observe high porosity peaks; the biggest subdomain is more regular than the smaller ones (local defaults); in particular it contains no hole. We can conclude that this sample is fairly homogeneous.

From Figure 18b, we can observe that the flow contour of the velocity magnitude is mainly tubular as expected, the vessels being oriented in the z direction. We find the permeability tensor is the $\{x,y,z\}$ basis:

$$\overline{\overline{K}}_D = \begin{pmatrix} 1.44 & 0 & 0 \\ 0 & 4.08 & 0 \\ 0 & 0 & 7.51 \end{pmatrix} \times 10^{-11}\, m^2, \tag{30}$$

with the values of the eigenvalues and eigenvectors in Table 16. The anisotropy is comparable to the previous smaller samples.

4.5.5. Representative Element Volume considerations

The question is then: is the 600^3 cells subdomain enough to approximate the permeability of the whole sample?

First, subdomain 3 is homogeneous, which at first may looks good, but as we have seen before it does not have holes that the whole sample has. Cutting a smaller part of it should possess the same "imperfections". Secondly, it is interesting to plot the evolution of the diagonal permeability tensor elements, namely K_{xx}, K_{yy} and K_{zz} for the samples. From Figure 19, we can observe that the variation for K_{zz} and K_{yy} is less than 10% from subdomain 2 to subdomain 3. K_{xx} seems to vary, for more than 32%

from subdomain 2 to subdomain 3. It is therefore difficult to say if this subdomain size is a reasonable REV. In order to check the global behavior for the intermediate structures, we generate and analyze a sample of 350^3 voxel cut in the 600^3 one. The obtained permeability tensor is similar to those of subdomain 2 and 3.

To conclude on REV considerations, the whole imaged sample is of about 6 mm edges, while the diameter of the tree is between 3 to 4.5 meters (average values). Therefore, the permeability values may be strongly dependent on the sample position.

As the BGK-FVS tools is well adapted to deal with such complex geometry, a detailed and systematic study will be carried out in order to extract representative properties of the wood using several (i.e. sampled at different tree position) and bigger (i.e. constituting a "true" REV) samples.

5. Conclusion

We designed a kinetic BGK equation which corresponds to a hyperbolic system. Then, we used a transport-projection method to approximate the RHS of the designed BGK, enabling to use a moment-based equation rather than discrete velocities ones. As this method can be seen as a Flux Vector Splitting one, we analyzed the moment-based equation with the tools of the FVS method, without involving any kinetic model. The entropy is kept at each step of the formal developments, from the continuous scheme to the discrete level. Then, the consistency and accuracy of the BGK-FVS method for application to INSE equations leads to flux/moment derivative conditions. These latter are satisfied by adjusting a free parameter and eventually allows to obtain second-order accuracy. In other words, we controlled the known diffusivity of the discrete scheme by adjusting it to the physical viscosity. The stability analysis is ensured with the entropy, which imposes that the computed moments remain in the stability region of the open set of admissible moments. Finally, the discrete entropy inequality holds under three different stability conditions: one coming from the CFL of the time discretization of the hyperbolic system, two from the stability region: the cell Reynolds number and the sub-characteristic condition. This means that the grid size must be small enough to satisfy all of them. However, the implementation requires less memory consumption than a discrete velocities approach, eventually the explicit scheme insure the good scalability of parallel software implementation.

We have shown that this new numerical scheme is well suited for accurate calculation of pressure and velocity field and find natural application in determination of macroscopic properties of complex geometries samples. Current numerical results showed that the new method characterizes precisely the Darcian permeability tensors, demonstrating its accuracy and robustness, for various porous media, from high to low porosities, both natural and manufactured media such as wood, soil or metallic foams. Those 3D complex structures may come from either binarized microtomographic images or CAD geometry,

which can have small imperfections, leading to meshing difficulties for commercial software. Moreover, such softwares use numerical schemes that may have difficulties in presence of isolated -closed- pores. We have seen that the BGK-FVS method does not have these two problems, showing excellent results in different media. In the present form, our proposed method is limited to intrinsic permeability of different porous media. The development of inertial effects is currently under development and will be presented in the near future.

Acknowledgement

We would like to thank Daniela BAUER for sending us the microtomographic images used in (L. Talon et al, 2006). This work was granted access to the HPC resources of Aix-Marseille Université financed by the project Equip@Meso (ANR-10-EQPX-29-01).

References

Aidun C.K., and Clausen J.R., 2010, “Lattice-Boltzmann Method for Complex Flows”. Annu. Rev. Fluid 42. DOI: 10.1146/annurev-fluid-121108-145519

Bardos C., Golse F., and Levermore C.D., 1993, “Fluid dynamic limits of kinetic equations-II Convergence proofs for the Boltzmann-equation”. Comm. Pure Appl. Math. 46, pp. 667-753

Bear J., 1972, Dynamics of Fluids in Porous Media. Dover publications

Bernsdorf J.,2008, “Simulation of complex flows and multi-physics with the lattice-boltzmann method”. PhD thesis. Amsterdam’s Univerity, p.114, p. 76

Boghosian B. and Levermore C., 1987, “A cellular automaton for Burgers’s equation”. Complex Systems 1, pp. 17-30

Bonnet J.P., Topin F., and Tadrist L., 2008, “Flow laws in metal foams: compressibility and pore size effects”. Transport in Porous Media 73 pp. 233-254

Bouchut F., 1999, “Construction of BGK Models with a Family of Kinetic Entropies for a Given System of Conservation Laws”. Journal of Statistical Physics 95.1-2, pp. 113-170

Bouchut F., Guarguaglini F.R., and Natalini R., 2000, “Diffusive bgk approximations for nonlinear multidimensional parabolic equations”. Indiana Univ. Math. J. 49, pp. 723-749

Bouchut F., 2002, “Entropy satisfying flux vector splittings and kinetic BGK models”. Numerische Mathematik 94.4, pp. 623-672

Bouchut F. and Frid H., 2006, “Finite difference schemes with cross derivatives correctors for multidimensional parabolic systems”. J. Hyp. Diff. Eq. 3, pp. 27-52

Bouchut F., Jobic Y., Natalini R., Occelli R., Pavan V., 2018, “Second-order entropy satisfying BGK-FVS schemes for incompressible Navier-Stokes equations”. SMAI-Journal of computational mathematics, 4, p. 1-56, doi: 10.5802/smai-jcm.28

Brun E., Vicente J., Topin F., and Occelli R., 2008, “IMorph: A 3D morphological tool to fully analyse all kind of cellular materials”. Cellmet08 Dresden, Germany

Brun E., Vincente J., Topin F., Occelli R., and Clifton M.J., 2009, “Microstructure and Transport Properties of Cellular Materials: Representative Volume Element”. Advanced material Engineering 11, pp. 805–810

Chen G.Q., Levermore C.D., and Liu T.-P., 1994, “Hyperbolic conservation laws with stiff relaxation terms and entropy”. Comm. Pure Appl. Math. 47, pp. 787-830

Chikatamarla S. and Karlin I., 2009, “Lattices for the lattice Boltzmann method”. Phys. Rev. E 79, p. 046701

Clague D. S., Kandhai B. D., Zhang R., 2000, “Hydraulic permeability of (un)bounded fibrous media using the lattice Boltzmann method”. Phys. Rev. E 61, pp. 616–625

Darcy H. P. G., 1856, “Exposition et application des principes à suivre et des formules à employer dans les questions de distribution d'eau. Les fontaines publiques de la ville de Dijon”. Paris, Victor Delmont

Elton B., Levermore C., and Rodrigue G., 1995, “Convergence of convective-diffusive lattice Boltzmann methods”. SIAM J. Numer. Anal. 32, pp. 1327–1354

Ergun S., 1952, “Fluid flow through packed columns,” Chem. Engineering Progress, vol. 48, pp. 89-94

Liu H., Kang Q., Leonardi C.R., 2015, “Multiphase lattice Boltzmann simulations for porous media applications”. Computational Geosciences, pp. 1-29

Hugo J-M, 2012, “Transferts dans les milieux cellulaires à forte porosité”. PhD thesis. Université Aix-Marseille.

d’Humières D., 1992, “Generalized lattice-Boltzmann equations in Rarefied Gas Dynamics: Theory and Simulations”. AIAA Progress in Astronautics and Astronautics 159, pp. 450-458

d’Humières D., Ginzburg I., Krafczyk M., Lallemand P., and Luo L.S., 2002, “Multiple-relaxation-time lattice Boltzmann models in three dimensions”. Phil. Trans. Royal Soc. London series A-Math. Phys. Eng. Sci. 360,pp. 437-451

Inamuro T., Yoshino M., and Ogino F., 1997, “Accuracy of the lattice Boltzmann method for small Knudsen number with finite Reynolds number”. Phys. Fluids 9, p. 3535

Jin S., Pareschi L., and Toscani G., 1998, “Diffusive relaxation schemes for multiscale discrete-velocity kinetic equations”. SIAM J. Numer. Anal. 35, pp. 2405-2439

Jobic Y., 2016, “Numerical approach by kinetic methods of transport phenomena in heterogeneous media”. PhD thesis. Université Aix-Marseille.

Karlin I.V., Gorban A.N., Succi S., and Boffi V., 1998, “Maximum entropy principle for lattice kinetic equations”. Phys. Rev. Lett. 81, pp. 6–9

Kumar P. and Topin F., 2014, “Micro-structural Impact of Different Strut Shapes and Porosity on Hydraulic Properties of Kelvin-Like Metal Foams”. Transport in Porous Media 105.57-81

Kumar P, Topin F, 2017, “Predicting pressure drop in open-cell foams by adopting Forchheimer number”. International Journal of Multiphase Flow 94, 123-136

Krook M., Bhatnagar P.L., Gross E.P., 1954, “A model for collision processes in gases”. Phys. Rev. 94, p. 511

Lallemand P. and Luo L.S., 2000, “Theory of the lattice Boltzmann method: dispersion, dissipation, isotropy, Galilean invariance, and stability”. Phys. Rev. E 61, pp. 6546-6562

Levermore D., Bardos C.; Golse F., 1991, “Fluid dynamical limits of kinetic equations, I : Formal derivation”. J. Statist. Phys. 63, pp. 323-344

McNamara G.R. and Zanetti G., 1988, “Use of the Boltzmann-equation to simulate lattice-gas automata”. Phys. Rev. Letters 61, pp. 2332-2335

Mandal J.C. and Deshpande S.M., 1989, “Higher order accurate kinetic flux vector splitting method for Euler equations, in Nonlinear Hyperbolic Equations – Theory, Computation Methods, and Applications”. Notes on Numerical Fluid Mechanics Series 24, pp. 384-392

METFOAM, 2015, international conference on porous media and metallic foams. Barcelona

Narváez A., Zauner T., Raischel F., Hilfer R., and Harting J., 2010, “Quantitative analysis of numerical estimates for the permeability of porous media from lattice-Boltzmann simulations”. Journal of Statistical Mechanics: theory and experiment P11026

Natalini R., Carfora M., 2008, “A discrete kinetic approximation for the incompressible Navier-Stokes equations”. ESAIM: M2AN 42, pp. 93-112

Pullin D.I., 1980, “Direct simulation methods for compressible inviscid idealgas flow”. J. Comput. Phys. 34, pp. 231-244

Renard P., Genty A., and Stauffer F., 2001, “Laboratory determination of the full permeability tensor”. J. Geophysical Res. 106.B11, pp. 26443-26452

Reitz R.D., 1981, “One-dimensional compressible gas dynamics calculations using the Boltzmann equations”. J. Comput. Phys. 42, pp. 108-123

Soulaine C., Quintard M., 2014, “On the use of a Darcy–Forchheimer like model for a macro-scale description of turbulence in porous media and its application to structured packings”, International Journal of Heat and Mass Transfer 74 88–100

Succi S., Foti E., and Higuera F., 1989, “3-dimensional flows in complex geometries with the lattice Boltzmann method”. Europhys. Letters 10, pp. 433-438

Succi S., 2001, “The lattice Boltzmann equation for fluid dynamics and beyond. Numerical Mathematics and Scientific Computation”, Oxford Science Publications, the Clarendon Press, Oxford University Press, New York

Succi S., Karlin I.V., and Chen H., 2002, “Role of the H theorem in lattice Boltzmann hydrodynamic simulations”. Rev. Mod. Phys. 74, pp. 1203-1220

Talon L., Bauer D., Gland N., Youssef S., Auradou H., and Ginzburg I., 2006, “Assessment of the two relaxation time Lattice-Boltzmann scheme to simulate Stokes flow in porous media”. Water Resources Research 48.4

Vicente J., Topin F., Daurelle J-V., and Rigollet F., 2006, “Thermal conductivity of metallic foam: simulation on real X-ray tomographied porous medium and photothermal experiments”. IHTC13, 13TH International Heat Transfer Conference, Sydney

Whitaker S., 1986, “Flow in porous media 1: a theoretical derivation of Darcy’s law”. Transport in Porous Media, vol. 1, pages 3–25

Yong W.A. and Luo L.S., 2005, “Nonexistence of H theorem for some lattice Boltzmann models”. J. Stat. Phys. 121, pp. 91-103

Zinszner B. and Pellerin F.M., 2007, “A geoscientist’s guide to petrophysics”. IFP Publication

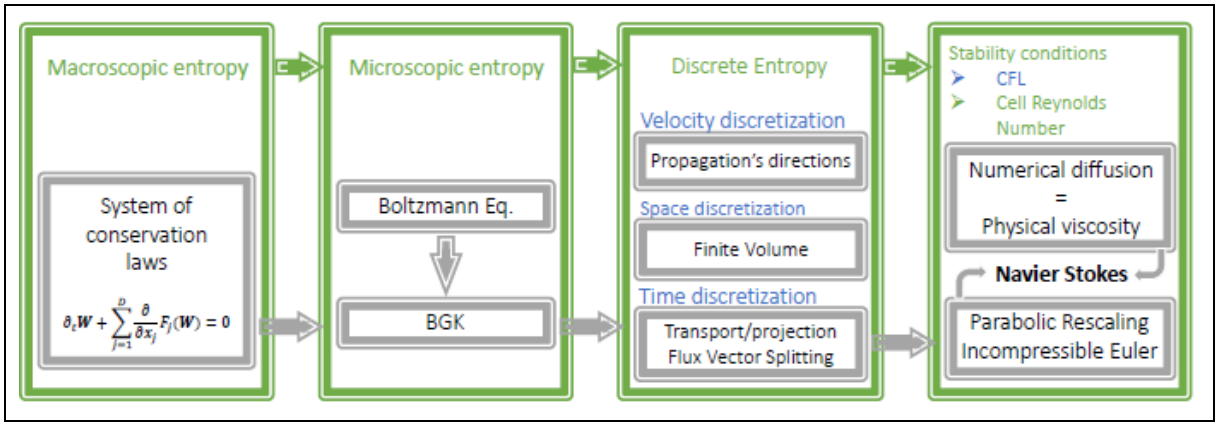

Figure 1: Block-diagram of the FVS-BGK scheme: A hyperbolic system of conservation laws is solved by a kinetic method using a BGK operator. The RHS of the designed BGK is approximated by a transport/projection algorithm, which can be interpreted as a flux vector splitting, enabling a moment-based scheme; the space discretization is done by a Finite Volume scheme, and the velocity discretization by a fixed set of discrete velocity. Then, after a parabolic rescaling we obtain the incompressible Euler equation, and diffusion is added by making a controlled numerical diffusion matching the physical viscosity, solving finally the Navier-Stokes equations. Entropy is conserved at each step, from the continuous scheme to the discrete level.

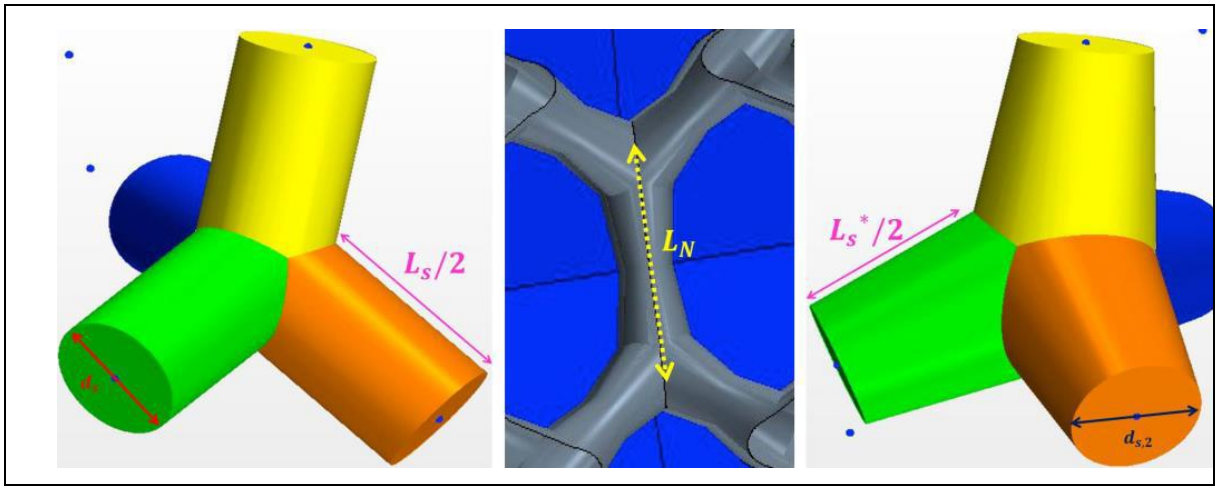

Figure 2: Presentation of a node and four struts of a foam sample (left) constant cross section of diameter, d_s and half strut length, $L_s/2$; (center) node to node length, L_N; (right) variable cross section of diameter, $d_{s,2}$ at the middle of the ligament and half strut length $L_s^*/2$.

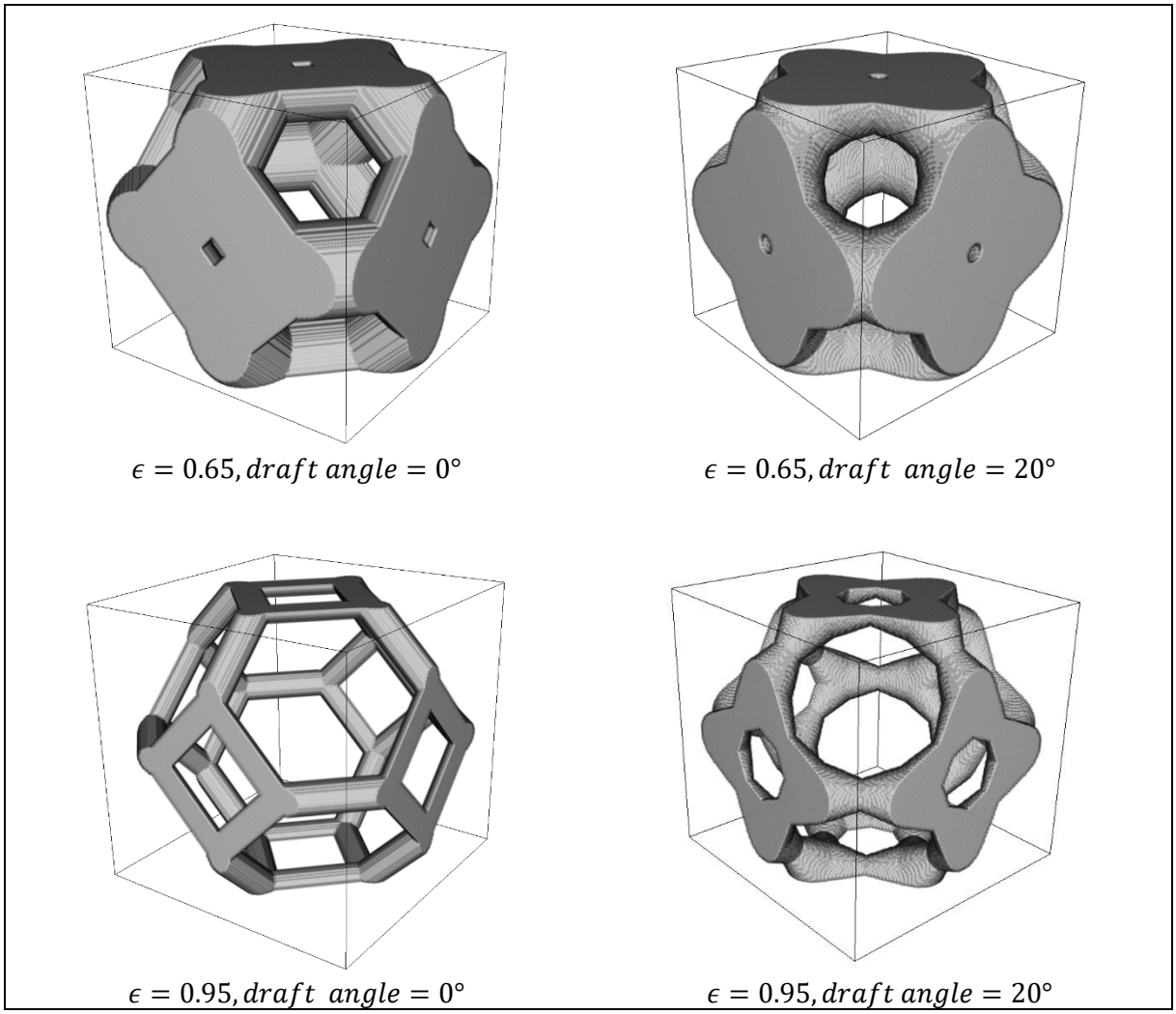

Figure 3: Left: constant struts diameter Kelvin-like cell. Right: variable strut diameter Kelvin-like cell. All cases d_{cell} *=4mm (Mesh Resolution* 160^3 *points). Upon increasing the draft angle, solid phase accumulates preferentially in the vicinity of node rather than near the middle of strut cross-section.*

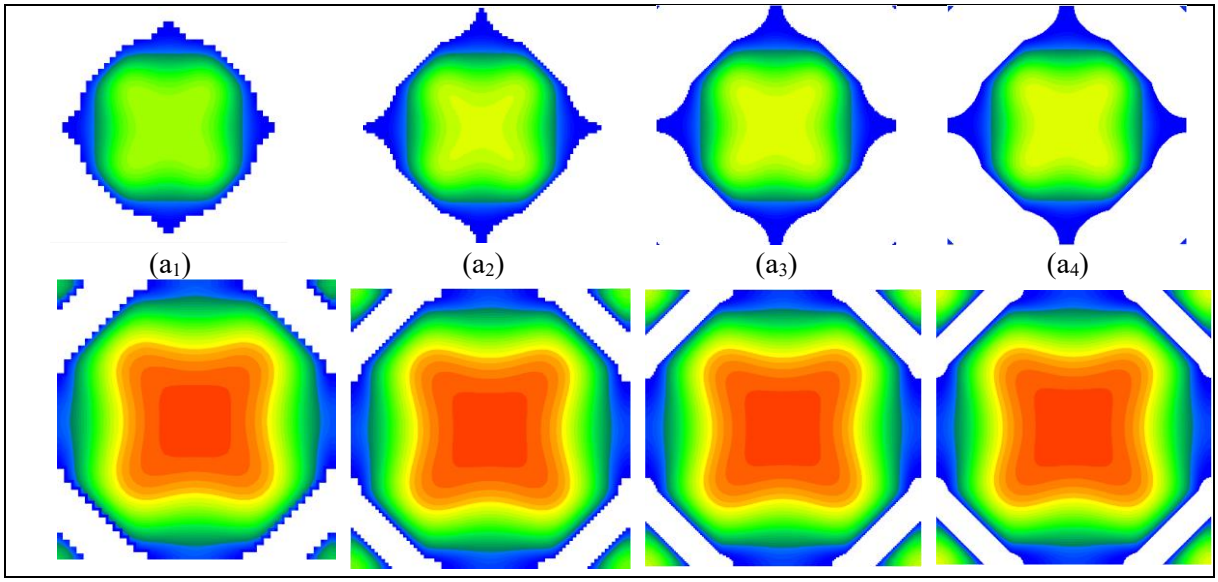

Figure 4: Velocity field in a cross section perpendicular to main flow axis located at the middle of a unit cell for various resolutions, from 40^3 to 320^3 voxels, and porosity (ϵ =0.6 up and 0.95 down)

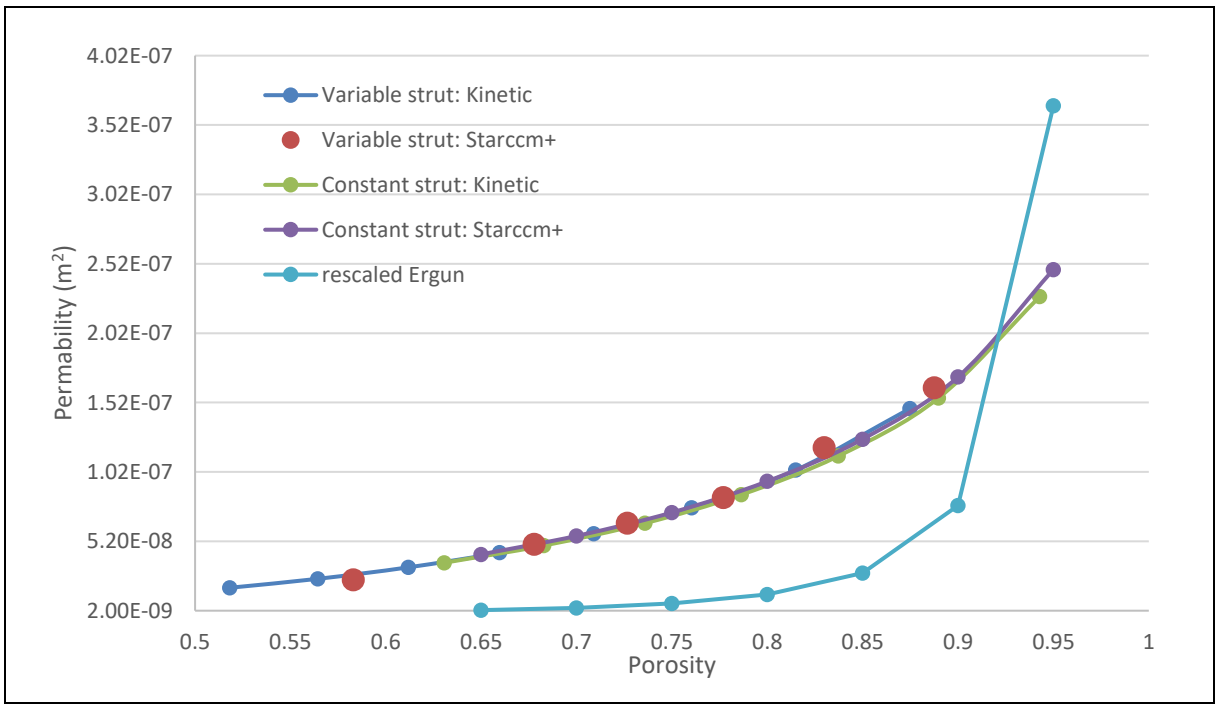

Figure 5: Validation and comparison of Darcian permeability variations as a function of porosity for a given cell size (d_{cell} =4mm), with variable and constant strut sections. Note that Ergun formula values are out of range and have been graphically rescaled in order to compare the shape of the curve with the actual data.

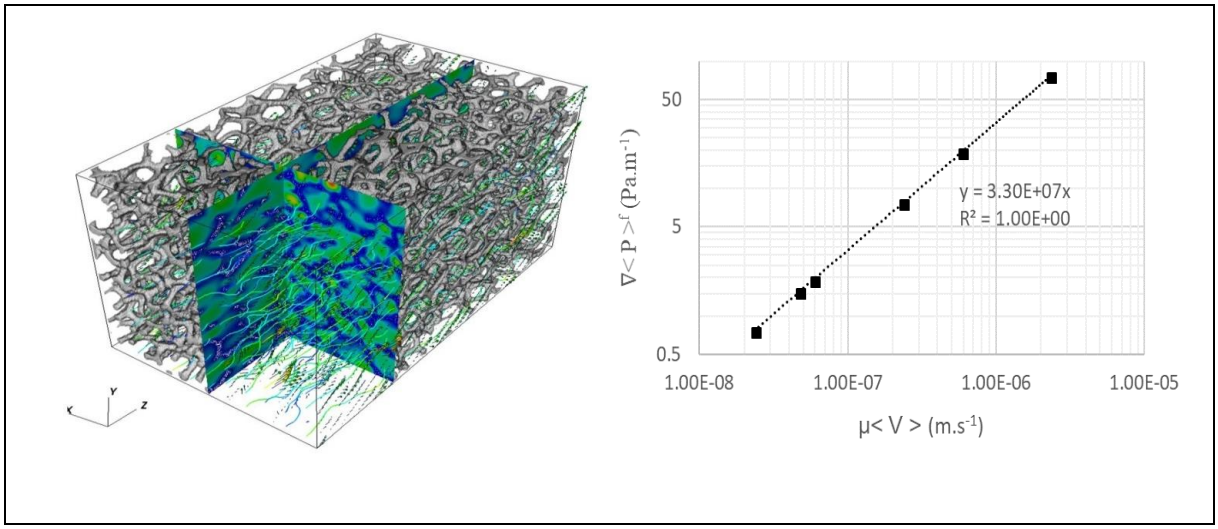

Figure 6. Left: 3-D reconstruction and flow field in a NC1723 foam sample (ε_o =0.87); Right: Extraction of permeability by linear regression and comparison with literature.

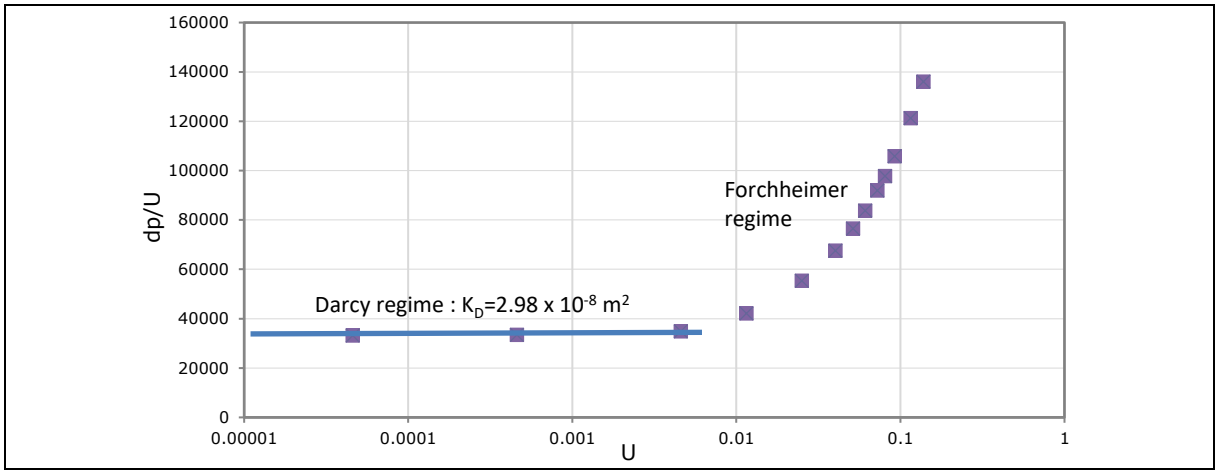

Figure 7: Delimitation of Darcy and Forchheimer regime for water in NC1723, data from the homemade Finite Volume code. Darcian Permeability value superimposed. Fluid water.

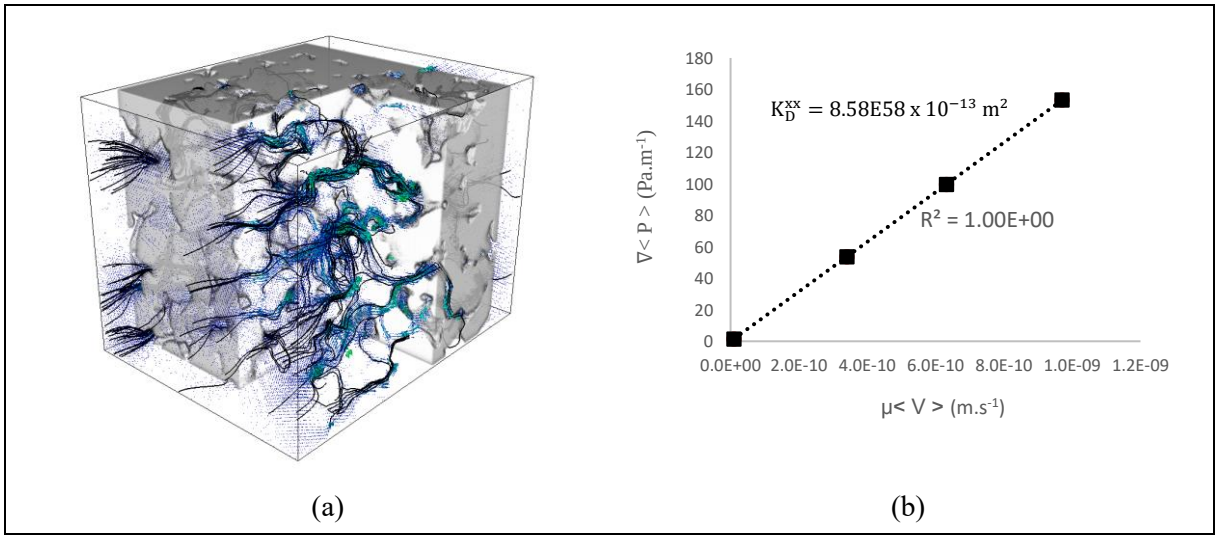

Figure 8: Permeability of a low porosity sandstone sample. (a) Pore scale calculated flow field. domain: $200 \times 200 \times 201$ *voxels,* $\epsilon = 13.5\%$*, (b) permeability determination, BGK-FVS data. We found an excellent linear fit, with* $R^2 = 1.0$

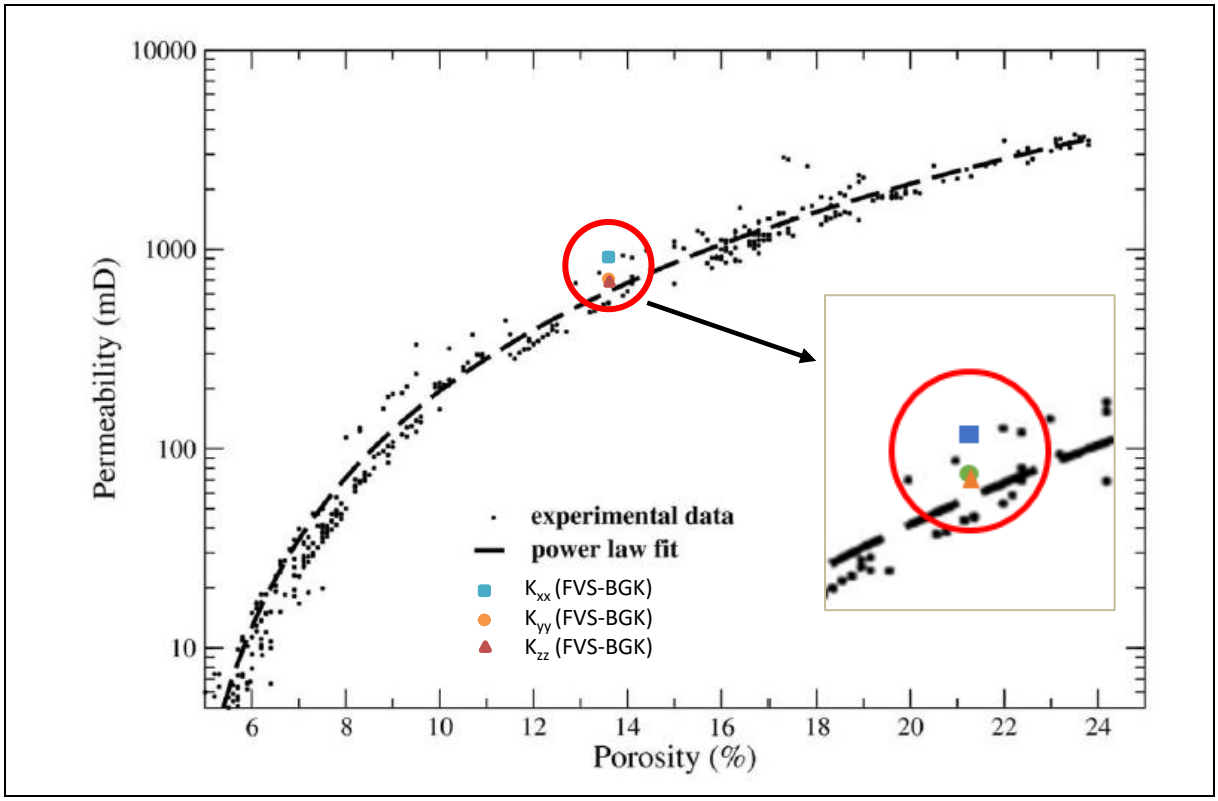

Figure 9: BGK-FVS permeability results compared to experimental data and literature correlation; sandstone sample of porosity 13.5%

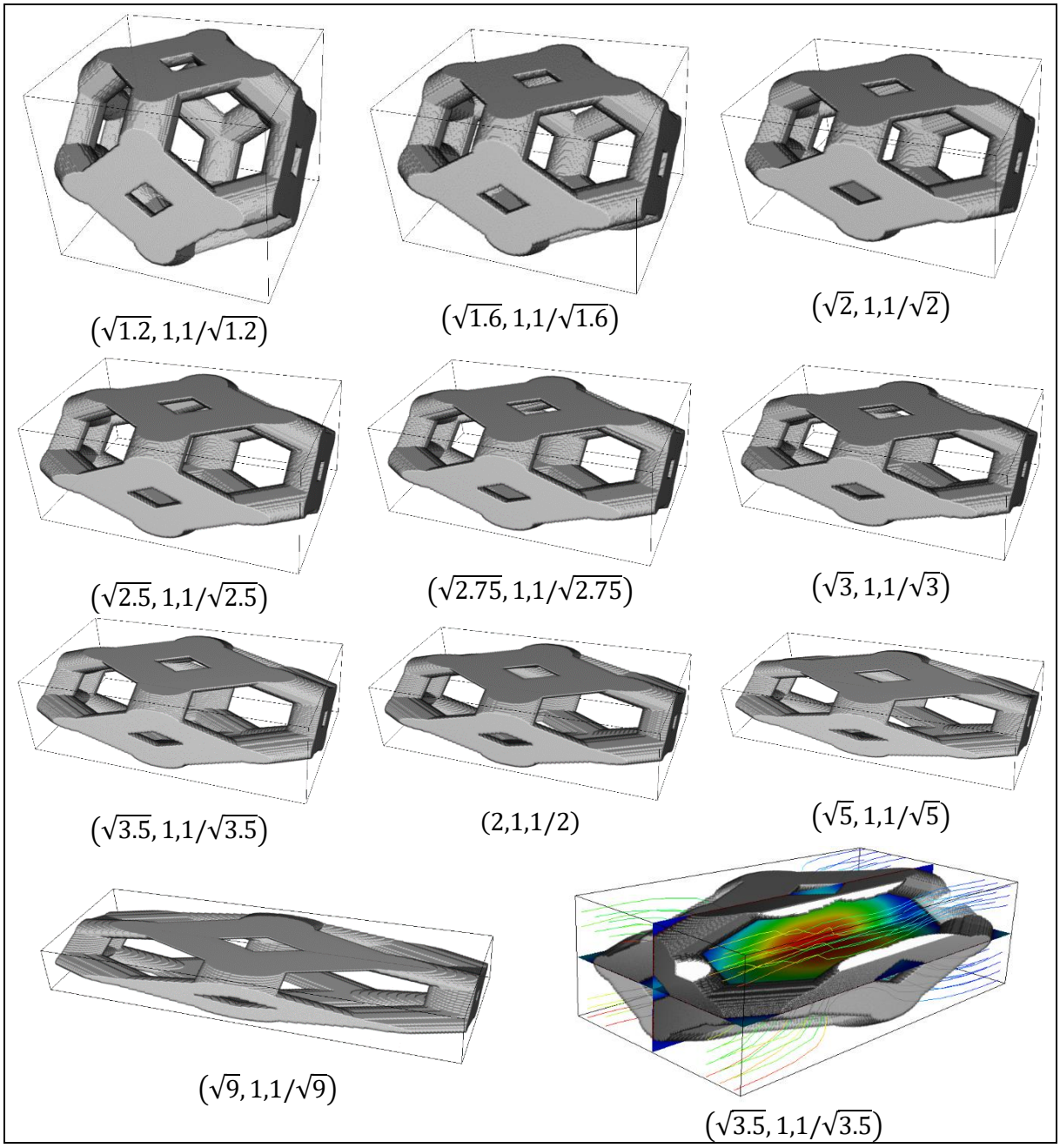

Figure 10: Kelvin-like samples (circular strut) for various elongations; Pore scale fluid flow result shown on the last figure (streamlines and velocity magnitude cut off)

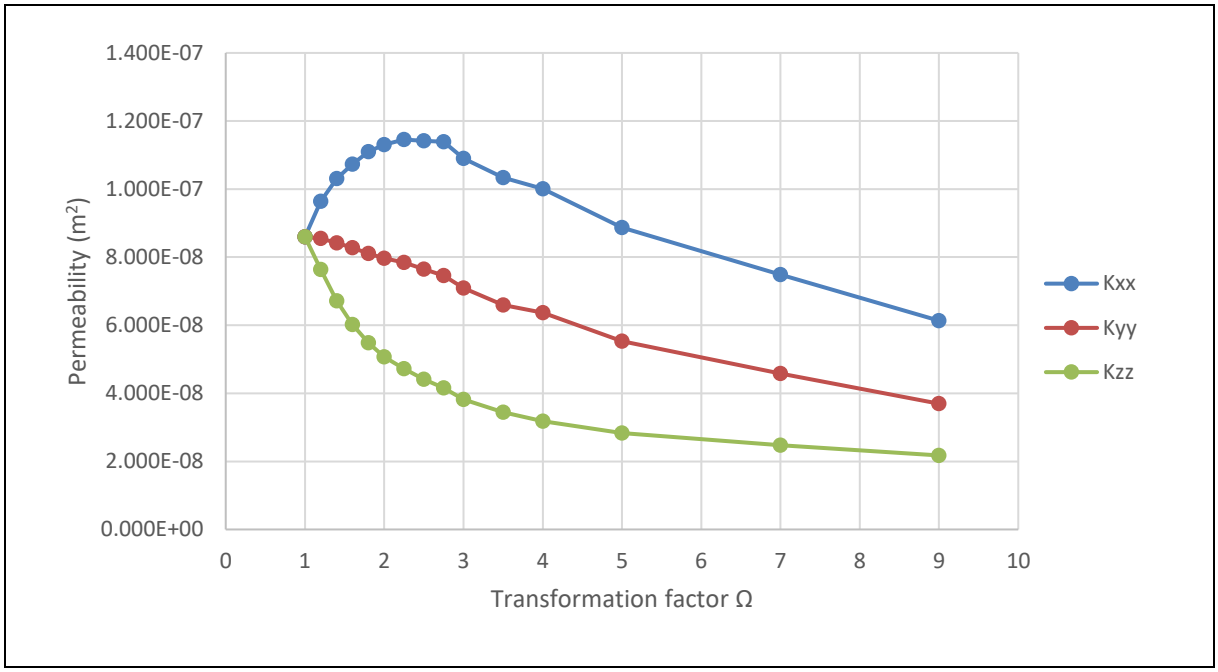

Figure 11: Permeability tensors diagonal components versus elongation factor Ω Kelvin like foam sample.

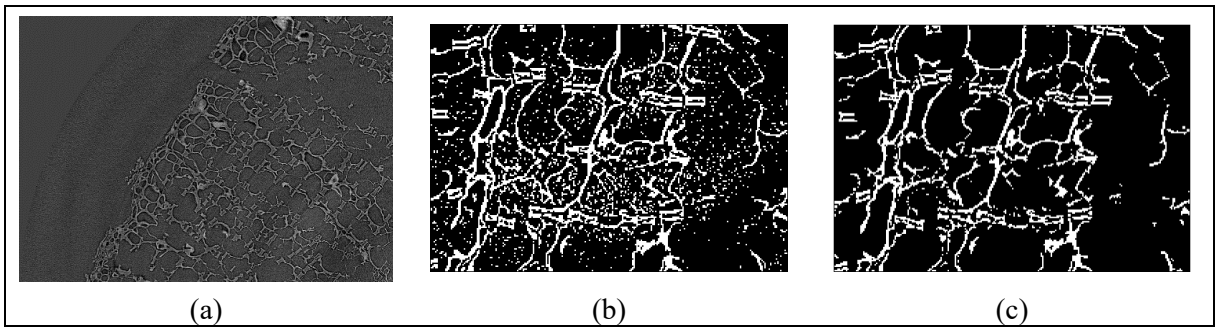

Figure 12: Redwood structure micro-tomographs (a) Raw image (b) Direct thresholding on the raw data-> gives a lot of false solid voxels (c) Thresholding after a cleaning stage (removal of non-connected components). The remaining small white voxels are connected to other slices.

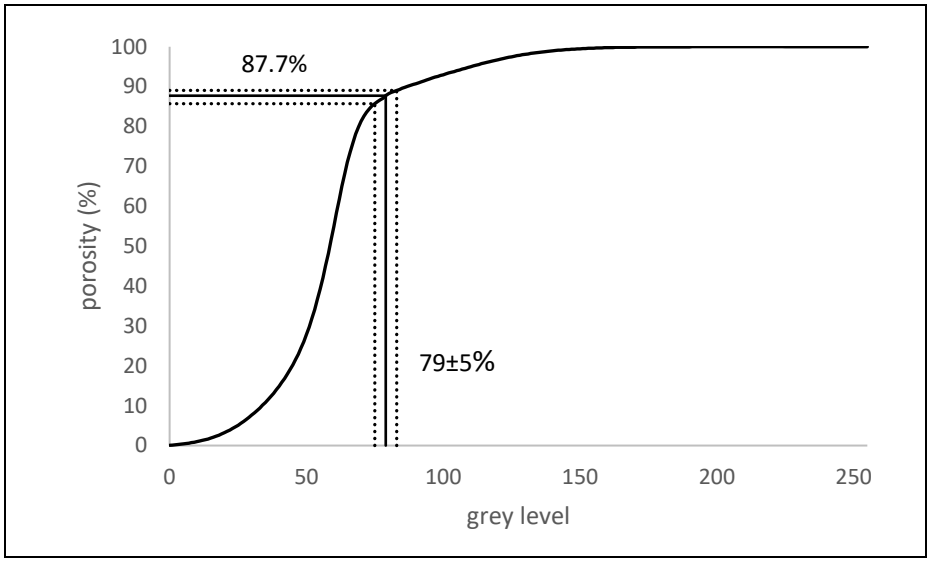

Figure 13: Impact of thresholding on porosity: sensibility study. For a threshold variation of 5%, we obtain a variation of about 2% of porosity in the vicinity of chosen threshold value.

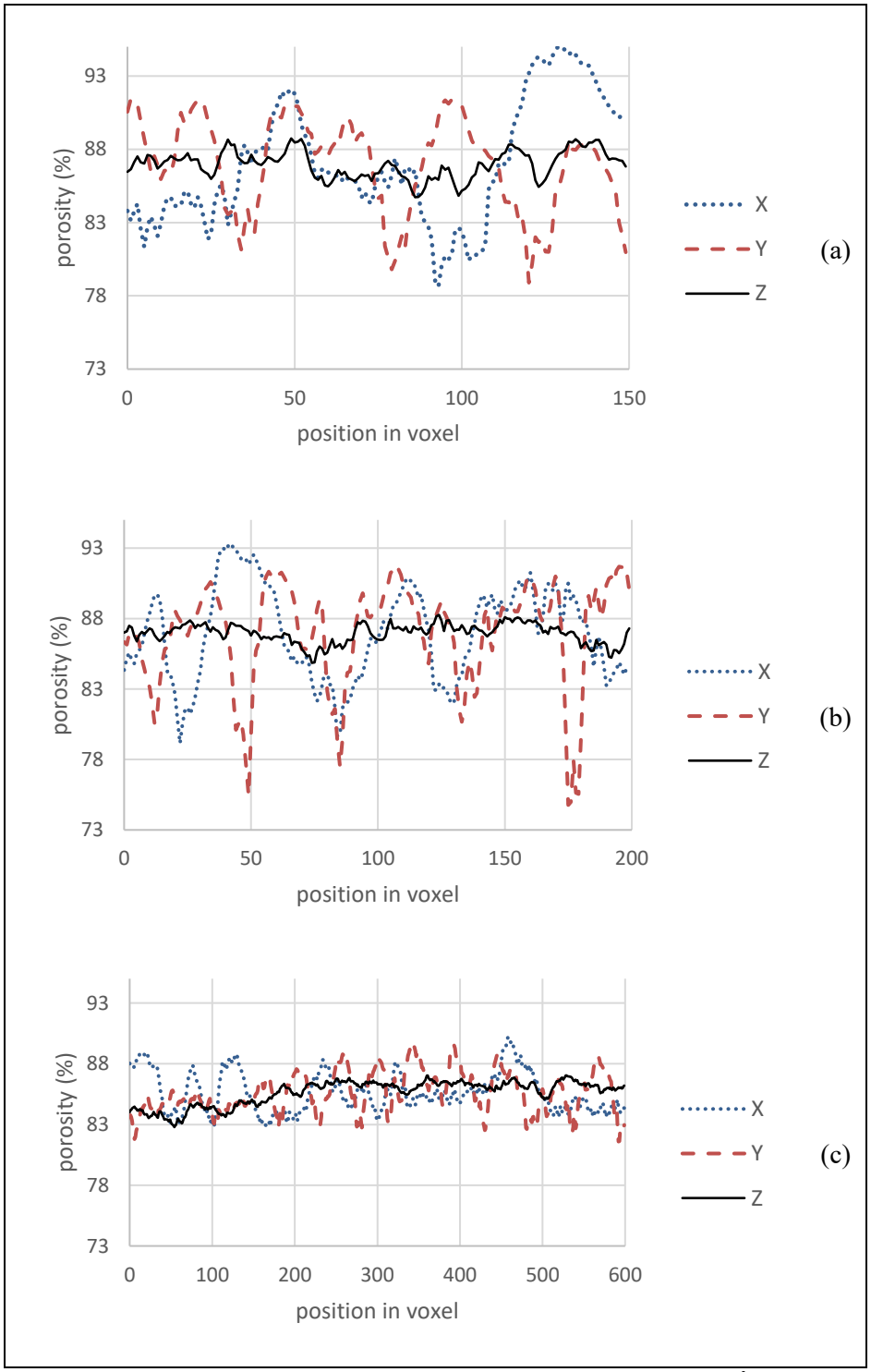

Figure 14: 2D Porosity variations along each direction: (a) subdomain 1(150^3 cells). The ***z*** *direction has less porosity variation than the other 2, giving the visual result that the wood fibers are oriented in this direction. (b) subdomain 2 (200^3 cells). Some small dense regions appear (c) subdomain 3 (600^3 cells). A more homogeneous distribution is observed.*

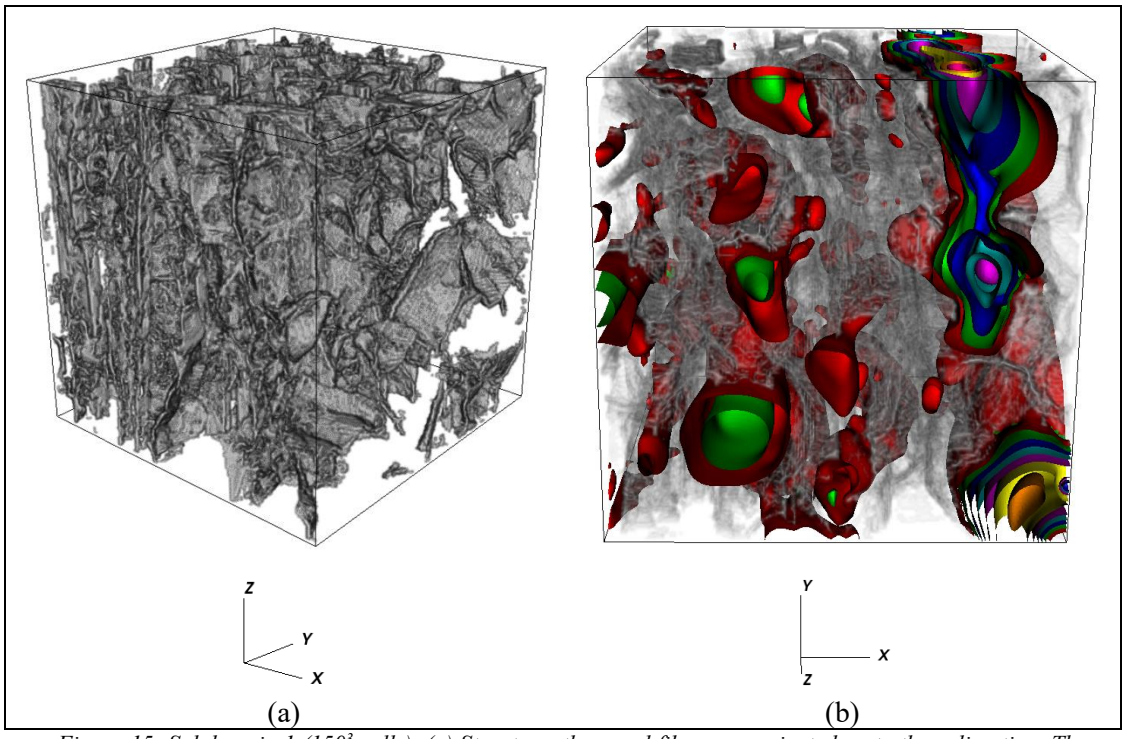

Figure 15: Subdomain 1 (150^3 cells). (a) Structure, the wood fibers are oriented up to the ***z*** *direction. There is a hole in the structure. (b) Pore scale flow pattern. The image view-angle is different; see the hole in the wood structure. 3D iso-contours of velocity magnitude. The main flow is in the same direction than the wood fibers. Pressure difference imposed along* ***z***

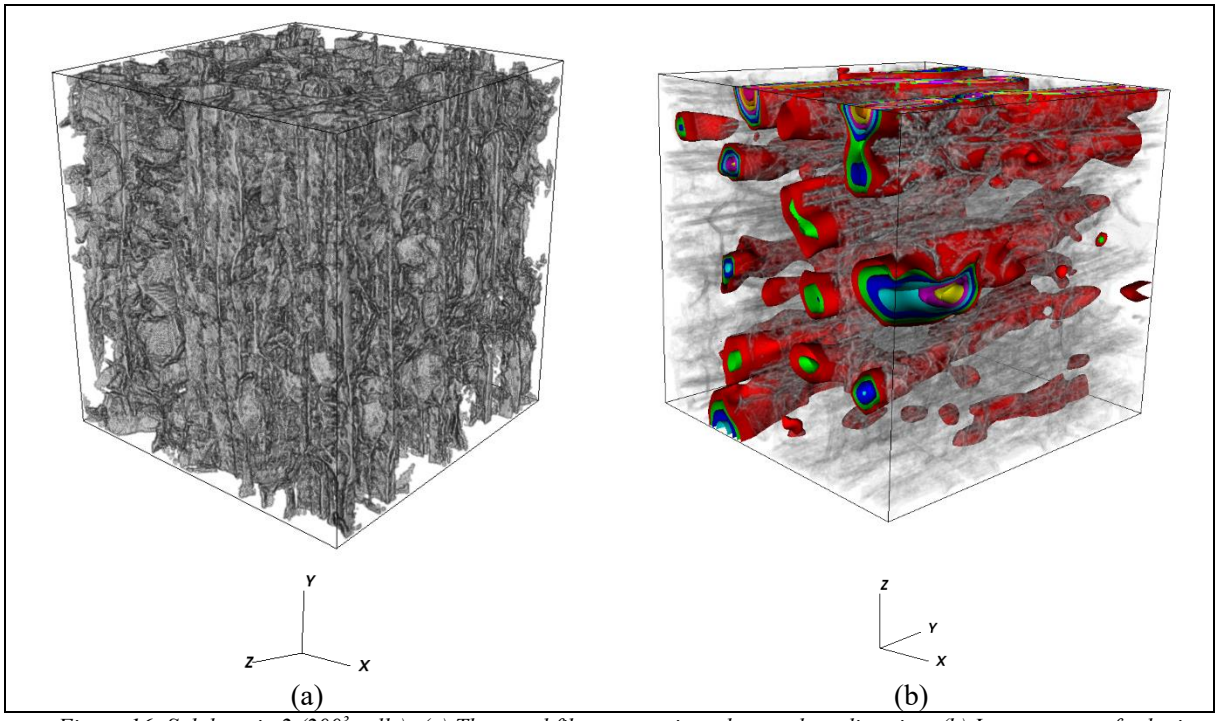

*Figure 16: Subdomain 2 (200^3 cells): (a) The wood fibers are oriented up to the **z** direction. (b) Iso-contours of velocity magnitude for a different view-angle. The flow presents a tubular aspect as expected from the vessels structure. Pressure difference imposed along **z***

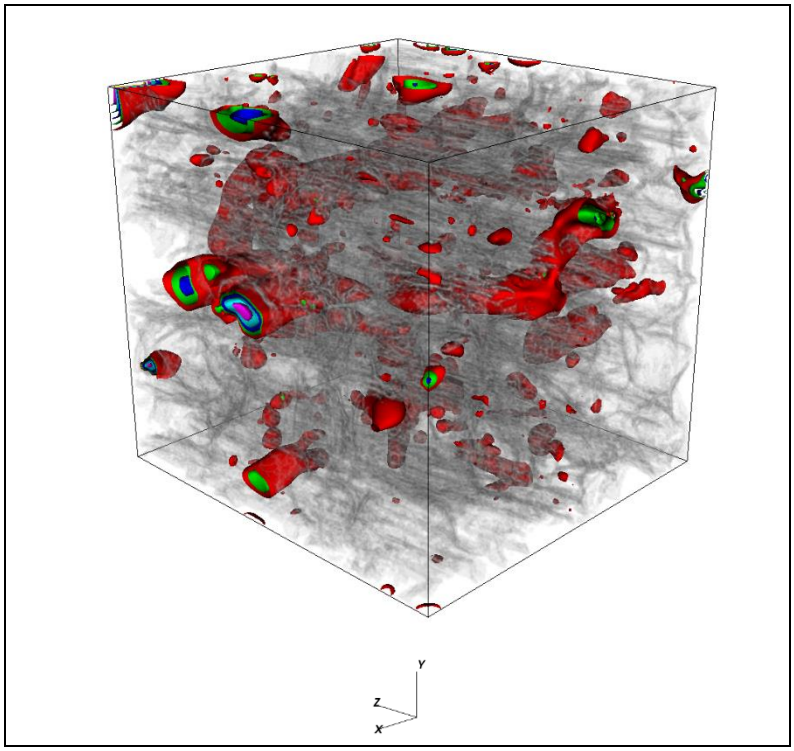

Figure 17: Subdomain 2. Iso-contours of velocity magnitude for a different view-angle. The flow presents a rather convoluted path. Pressure difference imposed along ***x****.*

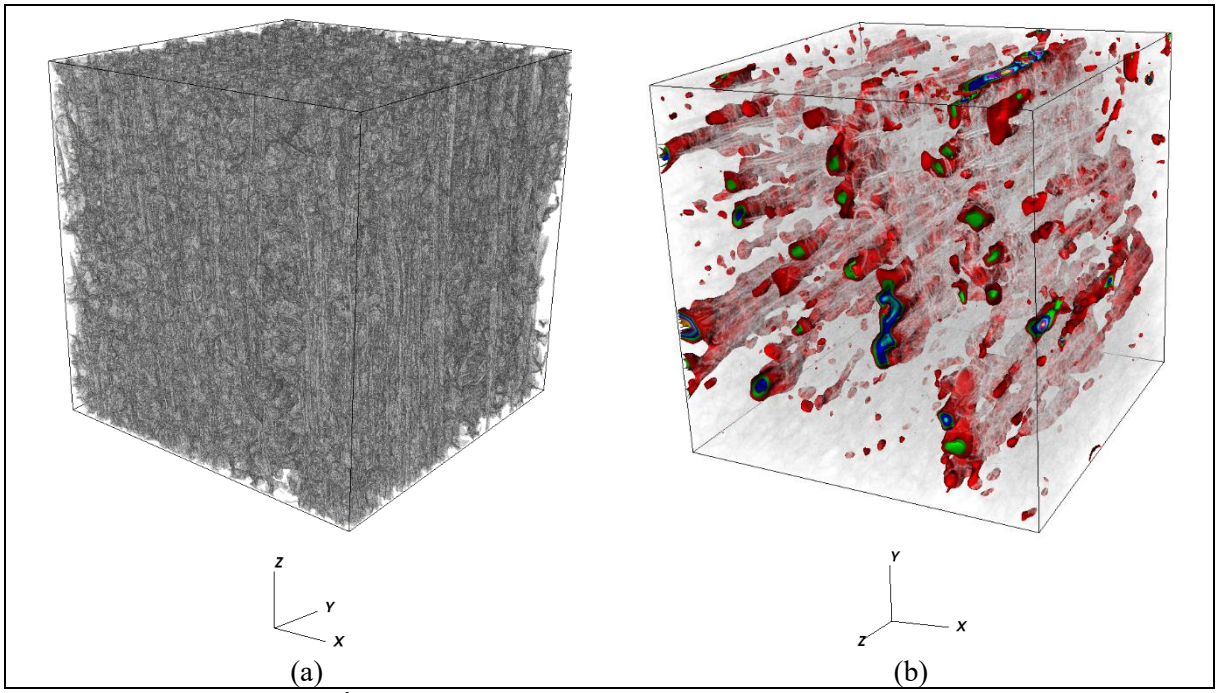

Figure 18: Subdomain 3 (600^3 cells). (a) The wood fibers are oriented up to the ***z*** *direction. (b) Iso-contours of velocity magnitude for a different view-angle. The flow presents a tubular aspect as expected from the vessels structure. Pressure difference imposed along* ***z***

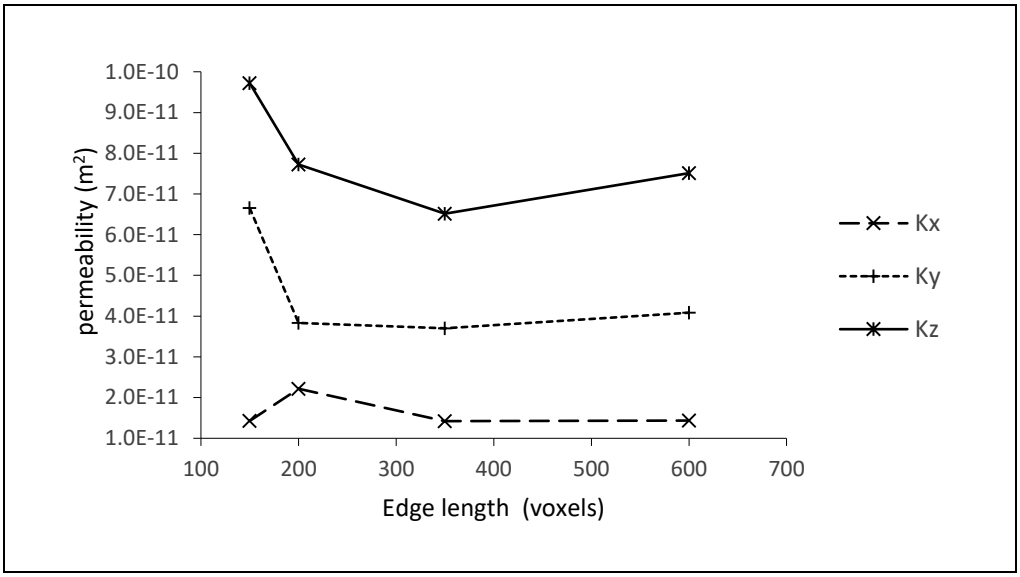

Figure 19: Evolution of the diagonal component of permeability tensor versus the subdomain size. Kz and Ky show good convergence, whereas Kx seems to vary. Globally a REV size of 200^3 voxels seems acceptable.

Table 1: Eigenvalues and eigenvectors for the permeability tensor of the sandstone sample, direct extraction method without treatment $\overline{\overline{\boldsymbol{K}}}_{FT}$

$\lambda_1(10^{-13})$	$\boldsymbol{w_1}$	$\lambda_2(10^{-13})$	$\boldsymbol{w_2}$	$\lambda_3(10^{-13})$	$\boldsymbol{w_3}$
9.87	-0.941	7.71	-0.320	0.175	-0.110
	-0.163		0.853		0.496
	0.175		-0.037		-0.984

Table 2: Eigenvalues and eigenvectors for the permeability tensor of the sandstone sample, direct extraction method with small gradient cancelation $\overline{\overline{\boldsymbol{K}}}_{WSG}$

$\lambda_1(10^{-13})$	$\boldsymbol{w_1}$	$\lambda_2(10^{-13})$	$\boldsymbol{w_2}$	$\lambda_3(10^{-13})$	$\boldsymbol{w_3}$
9.87	-0.941	7.71	-0.320	7.43	-0.110
	-0.163		0.853		0.496
	0.175		-0.037		-0.984

Table 3: Eigenvalues and eigenvectors for the permeability tensor of the sandstone sample, forced symmetry extraction method $\overline{\overline{\boldsymbol{K}}}_{S}$

$\lambda_1(10^{-13})$	$\boldsymbol{w_1}$	$\lambda_2(10^{-13})$	$\boldsymbol{w_2}$	$\lambda_3(10^{-13})$	$\boldsymbol{w_3}$
9.92	0.970	7.71	0.202	7.37	0.135
	0.227		-0.951		-0.210
	0.086		0.234		-0.968

Table 4: Morphological parameters of virtual Kelvin-like foam, circular struts, constant cross-section.

$\varepsilon_o(-)$	$a_c\ (m^{-1})$	$d_p\ (mm)$	$d_s\ (mm)$
0.60	982	0.694	1.212
0.65	979	0.822	1.110
0.70	960	0.951	1.006
0.75	926	1.083	0.900
0.80	873	1.223	0.789
0.85	796	1.372	0.669
0.90	686	1.541	0.534
0.95	515	1.749	0.367

Table 5: Morphological parameters of various virtual Kelvin-like foam with variable cross-section of the struts.

$\theta(°)$	$d_{s,2}(mm)$	$\varepsilon_o(-)$	$a_c(m^{-1})$	$d_p(mm)$
2.5	0.7885	0.78	878.7	1.1298
5.0	0.7885	0.76	887.1	1.0786
7.5	0.7885	0.75	899.9	1.0402
10.0	0.7885	0.73	918.0	1.0125
12.5	0.7885	0.71	942.0	0.9940
15.0	0.7885	0.69	973.1	0.9841
17.5	0.7885	0.67	1012.5	0.9823
20.0	0.7885	0.65	1061.7	0.9884
2.5	0.3673	0.94	559.9	1.6297
5.0	0.3673	0.92	599.8	1.5498
7.5	0.3673	0.91	638.5	1.4889
10.0	0.3673	0.89	678.4	1.4443
12.5	0.3673	0.87	721.1	1.4132
15.0	0.3673	0.85	768.4	1.3945
17.5	0.3673	0.83	822.5	1.3875
20.0	0.3673	0.81	885.5	1.3919

Table 6: Mesh influence on morphology and permeability to quantify geometric discretization errors

	Resolution		Morphological properties		
Exact porosity sample	Voxel size (10^{-5} m)	Mesh cells	Porosity (ϵ_0)	Spe. Surface area, ac (m^{-1})	Permeability (10^{-7} m^2)
$\epsilon = 0.95$	10.0	403	0.938	754	2.28
	5.00	803	0.938	782	2.10
	2.50	1603	0.942	814	2.16
	1.25	3203	0.946	795	2.23
$\epsilon = 0.6$	10.0	403	0.533	1331	0.111
	5.00	803	0.567	1412	0.144
	2.50	1603	0.583	1440	0.160
	1.25	3203	0.591	1456	0.169

Table 7: Morphological parameters and permeability values of virtual foam samples (obtained with the FVS-BGK method).

	VFS-BGK		StarCCM+	
Type of foams	Porosity, ε_o $(-)$	Permeability, K_D $(10^{-8}\ m^2)$	Porosity, ε_o $(-)$	Permeability, K_D $(10^{-8}\ m^2)$
Foam samples based on constant strut diameter, angle 0°	0.631	3.65	0.65	4.26
	0.683	4.90	0.7	5.59
	0.736	6.50	0.75	7.28
	0.786	8.56	0.8	9.52
	0.837	11.30	0.85	12.56
	0.890	15.50	0.9	17.05
	0.943	22.80	0.95	24.79
Foam samples based on variable strut diameter, angle 20°	0.518	1.85		
	0.564	2.50	0.58	2.42
	0.612	3.32		
	0.660	4.38	0.68	4.98
	0.709	5.76	0.73	6.50
	0.760	7.63	0.78	8.35
	0.815	10.30	0.83	11.95
	0.875	14.80	0.89	16.26

Table 8: Eigenvalues and eigenvectors for the permeability tensor of the NC1723 sample

$\lambda_1(10^{-8})$	$\boldsymbol{w_1}$	$\lambda_2(10^{-8})$	$\boldsymbol{w_2}$	$\lambda_3(10^{-8})$	$\boldsymbol{w_3}$
3.32	-0.944 0.331 0	3.13	0.331 0.944 0.001	3.14	0 -0.001 1

Table 9: Eigenvalues and eigenvectors for the permeability tensor of the Fontainebleau sandstone sample

$\lambda_1(10^{-13})$	$\boldsymbol{w_1}$	$\lambda_2(10^{-13})$	$\boldsymbol{w_2}$	$\lambda_3(10^{-13})$	$\boldsymbol{w_3}$
	0.970		0.086		0.227
9.92	0.135	7.71	-0.968	7.36	-0.209
	0.202		0.234		-0.951

Table 10: Parameters of the experimental law

a	b	c	d
11.7	-40.29	51.6	-20.22

Table 11. Permeability values for the power law function (20) applied to different porosity values

	Porosity (ϵ)	Permeability (10^{-13} m^2)	confidence interval (10^{-13} m^2)
Sandstone core	14.5	7.17	[4.95,9.40]
μTomo sample	14.1	6.55	[4.52,8.58]
Computing domain	13.5	5.68	[3.92,7.44]

Table 12: Permeability diagonal terms of a virtual orthotropic foam sample for various elongations.

Ω (-)	ε_o (-)	${K_D}^{xx}$ (10^{-8} m²)	${K_D}^{yy}$ (10^{-8} m²)	${K_D}^{zz}$ (10^{-8} m²)
1	0.786	8.598	8.598	8.598
1.2	0.785	9.640	8.554	7.640
1.4	0.784	10.31	8.421	6.712
1.6	0.783	10.74	8.275	6.023
1.8	0.782	11.10	8.109	5.482
2	0.781	11.30	7.962	5.071
2.25	0.784	11.45	7.846	4.727
2.5	0.783	11.42	7.650	4.411
2.75	0.783	11.39	7.455	4.154
3	0.779	10.90	7.091	3.821
3.5	0.779	10.34	6.596	3.441
4	0.779	10.01	6.367	3.180
5	0.777	8.871	5.535	2.828
9	0.771	6.134	3.695	2.175

Table 13: General presentation of the studied wood samples

Name	Voxel size (10^{-6} m)	Porosity (%)	Edge size (10^{-4} m)
Sample 1	3.22	0.8699	4.83
Sample 2		0.8699	6.44
Sample 3		0.8562	19.3

Table 14: Eigenvalues and eigenvectors for the permeability tensor of the 150^3 cells redwood sample

$\lambda_1(10^{-11})$	$\boldsymbol{w_1}$	$\lambda_2(10^{-11})$	$\boldsymbol{w_2}$	$\lambda_3(10^{-11})$	$\boldsymbol{w_3}$
1.43	-0.988	6.65	-0.152	9.72	-0.014
	-0.146		0.969		-0.199
	-0.044		0.194		0.980

Table 15: Eigenvalues and eigenvectors for the permeability tensor of the 200^3 cells redwood sample

$\lambda_1(10^{-11})$	$\boldsymbol{w_1}$	$\lambda_2(10^{-11})$	$\boldsymbol{w_2}$	$\lambda_3(10^{-11})$	$\boldsymbol{w_3}$
2.22	-0.995	3.83	-0.093	7.72	0.037
	-0.094		0.994		-0.050
	0.032		0.053		0.998

Table 16: Eigenvalues and eigenvectors for the permeability tensor of the 600^3 cells redwood sample

$\lambda_1(10^{-11})$	$\boldsymbol{w_1}$	$\lambda_2(10^{-11})$	$\boldsymbol{w_2}$	$\lambda_3(10^{-11})$	$\boldsymbol{w_3}$
1.44	-0.991	4.08	-0.135	7.51	0.007
	-0.135		0.991		-0.009
	0.006		0.010		1.000